Unified Model for Contact Angle Hysteresis on Heterogeneous and Superhydrophobic Surfaces

Citation: Raj, Rishi, Ryan Enright, Yangying Zhu, Solomon Adera, and Evelyn N. Wang. "Unified Model for Contact Angle Hysteresis on Heterogeneous and Superhydrophobic Surfaces." Langmuir 28, no. 45 (November 13, 2012): 15777–15788.

As Published: http://dx.doi.org/10.1021/la303070s

Publisher: American Chemical Society (ACS)

Persistent URL: http://hdl.handle.net/1721.1/85199

Version: Author's final manuscript: final author's manuscript post peer review, without publisher's formatting or copy editing

Unified Model for Contact Angle Hysteresis on Heterogeneous and Superhydrophobic Surfaces

Rishi Raj[1], Ryan Enright[1,2], Yangying Zhu[1], Solomon Adera[1], and Evelyn N. Wang[1]*

[1]Department of Mechanical Engineering, Massachusetts Institute of Technology, Cambridge, MA, 02139 USA

[2]Stokes Institute, University of Limerick, Limerick, Ireland

*Corresponding Author: Address: 77 Massachusetts Ave., 3-461B, Cambridge, MA 02139

Email: enwang@mit.edu, Phone: (617)324-3311, Fax: (617)258-9346

KEYWORDS Contact Line Dynamics, Contact Angle Hysteresis, Heterogeneous Surface, Superhydrophobic Surface, Evaporation

ABSTRACT Understanding the complexities associated with contact line dynamics on chemically heterogeneous and superhydrophobic surfaces is important for a wide variety of engineering problems. Despite significant efforts to capture the behavior of a droplet on these surfaces over the past few decades, modeling of the complex dynamics at the three-phase contact line is needed. In this work, we demonstrate that contact line distortion on heterogeneous and superhydrophobic surfaces is the key aspect that needs to be accounted for in the dynamic droplet models. Contact line distortions were visualized and modeled using a thermodynamic approach to develop a unified model for contact angle hysteresis on chemically heterogeneous and superhydrophobic surfaces. On a surface comprised of discrete wetting defects on an

interconnected less wetting area, the advancing contact angle was determined to be independent of the defects while the relative fraction of the distorted contact line with respect to the baseline surface was shown to govern the receding contact angle. This behavior reversed when the relative wettability of the discrete defects and interconnected area was inverted. The developed model showed good agreement with the experimental advancing and receding contact angles, both at low and high solid fractions. The thermodynamic model was further extended to demonstrate its capability to capture droplet shape evolution during liquid addition and removal in our experiments and those in literature. This study offers new insight extending the fundamental understanding of solid-liquid interactions required for design of advanced functional coatings for microfluidics, biological, manufacturing, and heat transfer applications.

1. Introduction

Interactions between liquids and solids are ubiquitous in our physical environment and are typically characterized by the wetting angle that a liquid droplet makes on the solid surface[1]. When a pure liquid droplet is placed on a smooth chemically homogenous solid surface in an isothermal vapor-saturated environment, the contact angle is given by Young's equation[2]. However, in practical engineering applications, surfaces are typically rough[3] and heterogeneous[4], and the temperature and humidity are non-uniform[5]. Wenzel[3] modeled the equilibrium contact angle of droplets on chemically homogenous rough surfaces where the liquid completely wets the surface, $\cos\theta_W = r\cos\theta_Y$, where r is the roughness ratio defined as the actual area to the projected area of a surface, θ_Y is the Young's contact angle on a smooth chemically homogenous surface, and θ_W is the apparent contact angle on the rough surface. The apparent contact angle of a liquid droplet on such a surface either increases or decreases with roughness depending on the Young's contact angle being greater than or less than 90° on a chemically identical smooth baseline surface.

Subsequently, Cassie and Baxter[4] extended Wenzel's analysis to model a distinctly different case of droplets in equilibrium on porous (composite/heterogeneous) surfaces, $\cos\theta_{CB} = sf\cos\theta_{Y1} + (1-sf)\cos\theta_{Y2}$, where θ_{Y1} and θ_{Y2} are the Young's contact angle on the baseline homogenous surfaces, *sf* is the solid fraction of the surface demonstrating θ_{Y1} and θ_{CB} is the apparent contact angle on the heterogeneous surface. While these theories are widely used, there is ongoing debate concerning the applicability of these equilibrium models when used to capture dynamic droplet behavior[6-7]. In such cases, the contact angle can take on any number of values bounded by the two characteristic angles that are not predicted by the global equilibrium analysis. The upper limit of the contact angle is observed for an advancing contact line while the lower limit of the contact angle is observed at the receding contact line. The difference between the advancing and receding contact angles is referred to as contact angle hysteresis and is an important parameter for a number of practical applications[8].

Recent advances in synthesis techniques have enabled the fabrication of model surfaces with well-defined micro-/nano-scale heterogeneities[8f-p] to investigate the effect on contact angle hysteresis. In addition, with the ability to capture high resolution images, these studies have highlighted limitations in using the Cassie-Baxter (CB) equation to model the dynamic contact angle. Extrand[8i] demonstrated that the wetting behavior is determined by interactions at the three-phase contact line and not by the solid-liquid contact area by measuring the advancing and receding contact angles of a small sessile drop deposited on the center of a single chemically heterogeneous island[8j]. As liquid was sequentially added, the contact line advanced beyond the island perimeter onto the surrounding area where the advancing contact angle changed to the value exhibited on the homogeneous periphery, and was unaffected by the heterogeneity completely contained within the contact line. Gao and McCarthy[6, 8h] supported these observations and further

proposed that the advancing and receding contact angles are a function of the local activation energies that need to be overcome in order for the contact line to move.

In contrast to these observations, Li and Amirfazli[8q] proposed a two-dimensional free energy thermodynamic analysis for textured surfaces where the predicted equilibrium contact angles corresponded to the CB equation and were shown to be consistent with experimental observations. Similarly, McHale[7], after analyzing a random heterogeneous surface, suggested that even the local thermodynamic considerations eventually yield contact angles predicted by the CB equation. Furthermore, it was reasoned that since the droplet perimeter does not necessarily coincide with the three-phase contact line of a droplet resting on a superhydrophobic surface, the contact lines within the apparent contact perimeter are important in determining the observed contact angles. Yeh *et al.*[8f] performed contact angle hysteresis experiments with CB droplets on structured surfaces where the solid fraction was varied from 0.05 to 0.55. As with the previous studies[7, 8q], the experimental results were stated to be consistent with the theoretical predictions of the CB model. However, wide discrepancies were evident from their data where the CB model over-predicted ($\theta_{CB} - \theta_{exp}$~15°) the advancing and receding contact angles at low solid fractions and under-predicted ($\theta_{exp} - \theta_{CB}$~20°) them at high solid fractions. Additionally, the physical picture adopted in these studies where the area fraction dictates the contact angle implies that no hysteresis should be observed on a heterogeneous surface if the individual homogenous surfaces comprising the heterogeneous surface do not have intrinsic contact angle hysteresis. However, in reality, even if the individual homogenous regions have negligible hysteresis, significant hysteresis can be observed on a heterogeneous surface when the individual homogenous regions demonstrate significant differences in surface energies[9].

The discrepancies between the experiments and typical equilibrium approaches is attributed to the unaccounted role of contact line distortion on real heterogeneous surfaces, which has been demonstrated both with experiments[8k-m, 8r, s] and modeling[8m-p, 8r]. For example, Reyssat and Quéré[8k] performed experiments on hydrophobic, structured surfaces and found that the CB equation always under-predicted the experimentally observed contact-angle hysteresis[8k]. To explain this behavior, they developed a semi-empirical model inspired by the work of Joanny and de Gennes[8d], where the effect of contact line distortions were captured using a spring analogy. The developed model requires a fitting parameter and was stated to be valid only for well-defined strong (pinning) defects that are dilute such that each pillar distorts the contact line independently. Meanwhile, Choi *et al.*[8m] visualized the three-phase contact line distortion and accordingly modified the CB relationship using a local differential parameter in place of the global area/solid fractions. Recently, Yu *et al.*[10] investigated different defect shapes and proposed similar correction factors to the CB relationship. Even though the contact angle hysteresis prediction from these studies[8m, 10] explain the experimentally observed data better than the CB equation, these substitution parameters were not generalized to other cases since they were not rigorously derived using thermodynamic principles.

Despite significant interest and efforts devoted to increasing our understanding of the contact angle hysteresis phenomenon, a unified model that captures practical subtleties such as contact line distortion and is valid over a wide range of experimental conditions and geometric regimes, remains elusive. In this paper, we present a comprehensive physical model that was derived thermodynamically and accounts for the effect of local energy barriers. First, in section 2, the displacement of the three-phase contact line is visualized to confirm that contact line distortions on heterogeneous surfaces exist. The dynamic droplet with the distorted contact line evolves

through a series of quasi-equilibrium states, which we modeled using free energy minimization. Section 3 presents our detailed systematic experiments on surfaces with controlled defects spanning a wide range of area fractions and baseline wettabilities. The experimental results show excellent agreement with the model as discussed in section 4. In contrast to previous studies, our model accurately predicts contact angle hysteresis for all area fractions between the two extremes of the baseline homogenous surfaces. In section 5, we extend the model to predict droplet dynamics during evaporation to the ambient, which has important implications for applications such as automatic DNA mapping[11], and the self-assembly[12] and self-guided micro-/nano-patterning[13] of suspended particles. Our model, when coupled with accepted droplet evaporation models[14], is shown to identify the fraction of evaporation time spent in the contact line pinning mode, a piece of information critical for the above mentioned applications[11-13]. Finally, in section 6, we demonstrate the broad applicability of the work by comparing our model results with experimental data from literature for CB droplets on structured surfaces.

2. Contact Line Pinning and Distortion

In this section, the CB equation for idealized droplet behavior without contact line distortion on a heterogeneous surface is first derived to validate our thermodynamic approach. We then include the phenomenon of contact line distortion in the thermodynamic model to arrive at a more accurate formulation for predicting hysteresis. The model is next generalized to determine the contact angle hysteresis for the full range of solid fraction values and all combinations of intrinsic contact angles for baseline homogenous surfaces.

A droplet compensates the loss of liquid by either decreasing its contact angle where the base area remains unchanged due to the contact line pinning, or by shrinking its base area while

maintaining a constant receding angle. For a heterogeneous surface, the differential energy due to the volume loss if the droplet contact line were pinned is given as follows:

$$dE_P = \gamma_{lv}\, dA_{lv,P} = 2\,\pi R^2 \gamma_{lv}\, \frac{(1-2\cos\theta+\cos^2\theta)}{\sin\theta} d\theta \quad (1)$$

where γ_{lv} is the surface tension of the liquid, R is the droplet major radius, and θ is the instantaneous contact angle that the droplet makes with the surface. However, the differential energy for a droplet in the constant receding angle mode involves a solid-liquid area change (Figure 1) and requires accounting for the heterogeneity as follows:

$$dE_R = -(\gamma_{sv,1} - \gamma_{sl,1})\, sf P dQ - (\gamma_{sv,2} - \gamma_{sl,2})(1-sf) P dQ + 4\,\pi R \gamma_{lv}\,(1-cos\theta) dR \quad (2)$$

where $\gamma_{sl,i}$ and $\gamma_{sv,i}$ are the solid-liquid and solid-vapor interfacial tensions of the i^{th} surface comprising the heterogeneous surface and *sf* is the area fraction of defects. Assuming that the contact line on this heterogeneous surface is not distorted, the droplet perimeter is $P = 2\pi R\sin\theta$ and the change in base radius is $dQ = dR\sin\theta$. Substituting these in Eq. 2, the ratio between the differential energy terms in the pinning mode and constant receding angle mode accordingly is given by:

$$\frac{dE_P}{dE_R} = \left[\frac{2 - 3\cos\theta + \cos^3\theta}{-\cos\theta_{eff}\sin^2\theta \;+\; 2(1-\cos\theta)}\right] \quad (3)$$

where $\cos\theta_{eff} = sf\cos\theta_{Y1} + (1-sf)\cos\theta_{Y2}$, and θ_{Y1} and θ_{Y2} are the intrinsic contact angles of the domains "1" and "2" of the heterogeneous surface, respectively. Note, the detailed geometric manipulations required to derive Eq. 3 for a heterogeneous surface is similar to the corresponding analysis for a homogenous surface which is discussed in detail in the supplementary information (see section S1). If the instantaneous angle that a droplet makes with a surface θ at any time *t* is

larger than θ_{eff}, then $dE_P/dE_R > 1$, which implies that the pinning mode is thermodynamically favored over the receding mode. The instantaneous angle continues to decrease until it reaches θ_{eff} such that $dE_P/dE_R \leq 1$. At this point, the constant receding angle mode is thermodynamically favored resulting in contact line de-pinning and a constant contact angle of θ_{eff}. Since this analysis neglects the distortion of the contact line similar to McHale[7], the steady value of the dynamic contact angle, *i.e.*, receding in this case, is still governed by the area fraction "*sf*", and is essentially the classical CB equation[4]. Note that only the two extreme modes for volume loss, the contact line mode and the constant receding angle mode, were compared. A third mode where both the contact angle and the base area could change simultaneously is also conceivable. However, such a mixed mode is never thermodynamically favored over the two extreme modes provided the assumption that the droplet proceeds through a series of quasi-equilibrium states remains valid (see supplementary information section S1 and Figure S2 for details).

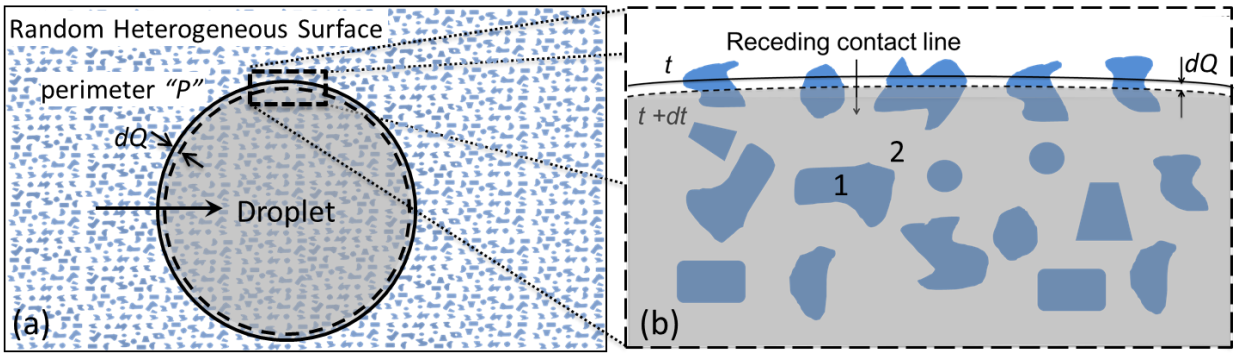

Figure 1. (a) A schematic of the undistorted contact line of a receding droplet on a random heterogeneous surface similar to McHale[7] along with a (b) magnified view of a rectangular area near the contact line (right). As the contact line recedes, the total solid-liquid area change in time *dt* is equal to the product *PdQ* of perimeter *P* and the change in droplet base radius *dQ*.

The situation shown in Figure 1, however, is over-simplified whereby in practical experiments, when the intrinsic contact angles on the two surfaces are different ($\theta_{Y1} \neq \theta_{Y2}$), the contact line in the advancing and receding modes is distorted. As a result, the above analysis cannot predict the experimentally observed dynamic contact angle values. Figure 2 shows time-lapse microscopy images of the contact line distortion behavior as a water droplet recedes on a heterogeneous surface with more hydrophilic defects. As can be seen from these images, the contact line is distorted along the more hydrophilic defects such that the droplet perimeter P is tortuous.

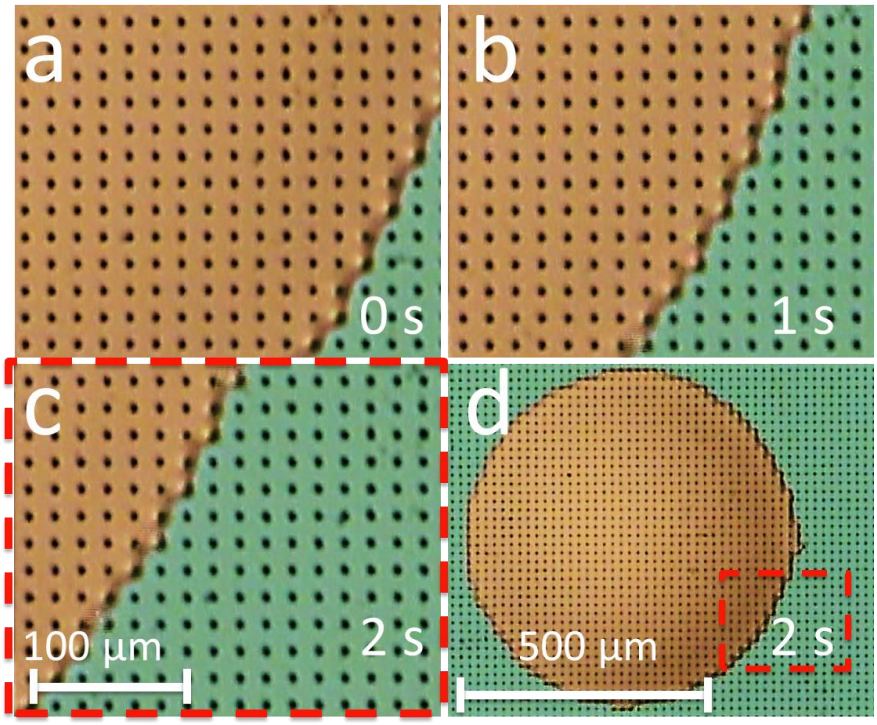

Figure 2. (a-c) Time-lapse optical microscope images of a receding droplet (θ_R ~ 4-8°) on SiO_2 surface patterned with photoresist dots. Distortions of the contact line are clearly shown along the more hydrophilic black dots as the contact line recedes. (d) A de-magnified view of the entire droplet corresponding to (c).

Contact line distortion results in local out-of-plane corrugations in the droplet profile. We approximate this behavior by assessing the differential energy ratio between the possible wetting configurations by formulating the problem using the contact line fraction instead of the actual contact line length. To explain the methodology developed to capture contact line distortions on a heterogeneous surface, we use an idealized example of a square array of circular defects (Figure 3) with diameter D and pitch L ($sf = \pi D^2/4L^2$). The circular domains "1" are more wetting than the background surface area ("2"), *i.e.*, $\theta_{Y1} < \theta_{Y2}$. We assume that both the domains are perfectly smooth and display no intrinsic contact angle hysteresis. In the receding mode, if the contact line completely lies on domain "2" and the instantaneous contact angle θ is larger than θ_{Y2}(time t_1, Figure 3a), the contact line will be pinned, *i.e.*, $dE_P/dE_R > 1$, until the angle θ equals θ_{Y2} and $dE_P/dE_R = 1$. The contact line can then recede with constant contact angle θ_{Y2} and $dE_P/dE_R = 1$ to a new position at time t_2. For the droplet to recede further, the contact line would need to sweep partially across the hydrophilic domain "1". For such a case, the value of dE_R as defined above would be lower than that compared to the case before where the contact line was positioned completely on domain "2". Considering that the value of dE_P is not dependent on the solid-liquid contact area, this essentially would imply an instantaneous increase in the ratio of differential energies ($dE_P/dE_R > 1$) resulting in the pinning mode. However, local thermodynamic considerations would allow the contact line to recede selectively on the domain "2" while the portion on the domain "1" remains pinned (Figure 3b, time t_3). If the local hydrophilic defects are small compared to the droplet size, this stage will be manifested as a global contact line pinning stage with an apparent contact angle dictated by the local contact line distortions. Distortions in the contact line can be defined by the angle β of the wetted perimeter on domain "1". The droplet subsequently proceeds through a series of quasi-steady states such that

the apparent contact angle decrease is compensated for by an effective increase in β and hence the contact line fraction $f = Dsin\beta/L$ on the defects. As a result, the energy ratio can be written as:

$$\frac{dE_P}{dE_R} = \left[\frac{2 - 3\cos\theta + \cos^3\theta}{-\cos\theta_{Y1}\frac{D\sin\beta}{L}\sin^2\theta - \cos\theta_{Y2}(1 - \frac{D\sin\beta}{L})\sin^2\theta + 2(1 - \cos\theta)}\right] \quad (4)$$

Unlike the previous case (Eq. 3) where the contact line was not distorted around defects and the fraction of differential area on "1" was equal to *sf,* the fraction of differential area on "1" due to a dQ displacement of the distorted contact line in the current case is equal to the instantaneous fraction *f* of the contact line on "1". The droplet then proceeds through a series of quasi-equilibrium states where $dE_P/dE_R \sim 1$ up to the point when $\beta = 90°$, after which the numerator dE_P cannot be larger than or equal to the denominator dE_R. The apparent contact angle at $\beta = 90°$ and $dE_P/dE_R = 1$ is manifested as the receding contact angle on such surfaces and can be expressed as:

$$\cos\theta_R = f_{max}\cos\theta_{Y1} + (1 - f_{max})\cos\theta_{Y2}, \quad (5)$$

where $f_{max} = D/L$ for the circular more hydrophilic defects. Any further volume loss from the droplet demonstrating $\theta = \theta_R$ will lead to the de-pinning ($dE_P/dE_R < 1$) of the contact line globally allowing the droplet to recede unobstructed with constant θ_R (Figure 3d). Thus, Eq. 5 represents a modified form of the CB equation that accounts for local contact line distortions. The contact line fraction on the defects is demonstrated to govern the contact line dynamics on heterogeneous surfaces. Unlike the previous approaches[8m, 10] where the area fraction in the CB equation was substituted by a defect shape dependent factor, this equation has been derived thermodynamically and can be generalized to other cases as shown in the subsequent discussion.

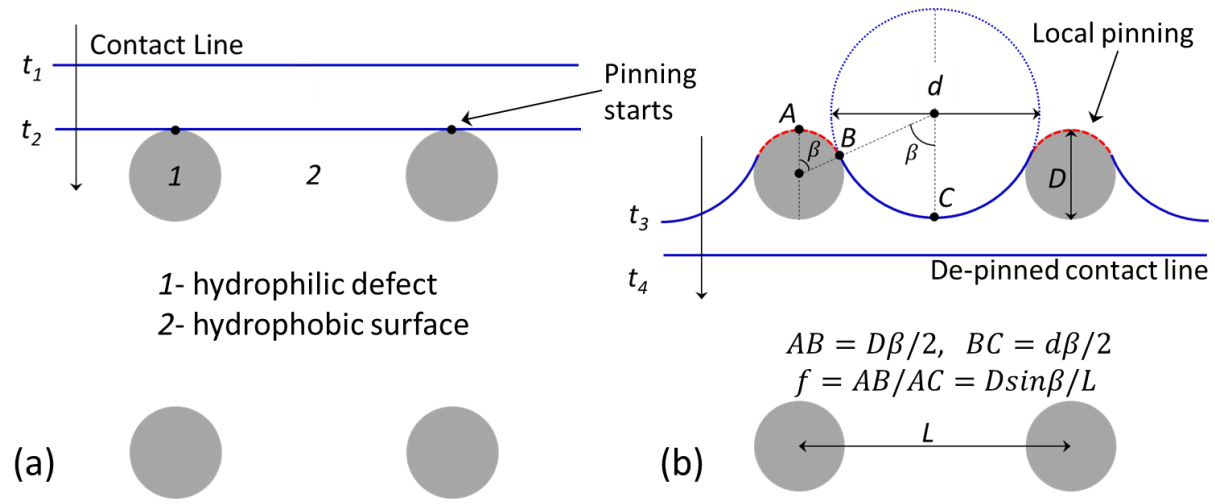

Figure 3. Schematic of the contact line movement (receding) on a background surface "2" with more wetting circular defects "1" in a square array. (a) The contact angle θ at time t_1 is equal to the Young's contact angle θ_{Y2} corresponding to the surface "2. The contact line recedes towards the next set of circular patterns at time t_2. The contact line can no longer move undistorted as the contact angle θ is larger than the Young's contact angle θ_{Y1} on these defects "1". (b) The droplet loses liquid such that the contact line becomes partially pinned on "1" while moving on "2", as shown at time t_3. The increase in the fraction of the contact line on "1" (f) results in an apparent decrease in contact angle ($\theta < \theta_{Y2}$). When the fraction of the contact line on the more wetting defects reaches the maximum value (f_{max}), the corresponding contact angle (θ_R) is the minimum contact angle after which any volume loss results in de-pinning and the constant receding angle mode. The contact line de-pins and moves unobstructed such that the contact angle remains constant (θ_R) afterwards (t_4).

Equation 5 shows that while the value of f_{max} increases with sf, it is always higher than sf indicating that the receding contact angle will be smaller than that predicted by the conventional CB equation[4]. Furthermore, the current model also suggests that the receding contact angle on a heterogeneous surface when $D/L \geq 1$, *i.e.*, the defects "1" are interconnected, is solely governed

by the wettability of defects ($\theta_R = \theta_{Y1}$). Note that the contact line fraction "f_{max}" required to overcome the local energy barrier should not be confused with the maximum value of f which can be 1. As is shown in the following discussion, a f_{max} of 0, *i.e.*, minimum value of f, may be required to overcome the local energy barrier if liquid is being added on similar surfaces. Conversely, if liquid is added, the key energy barrier will be encountered when the contact line lies completely on domain "2" (the interconnected less hydrophilic surface). Once this energy barrier is overcome, the contact line cannot pin and the advancing contact angle corresponds to the contact angle of the interconnected domain "2" (θ_{Y2}) independent of area fractions (for $0 \leq sf \leq 0.79$, $f_{max} = 0$). Hence,

$$\cos\theta_A = \cos\theta_{Y2}, \tag{6}$$

for discrete hydrophilic defects.

A schematic representation of the differential energies of the contact line pinning, constant receding angle, and constant advancing angle modes is shown on Figure 4. Although the contact line fraction, as explained above, is a dynamic parameter and changes progressively with contact line distortion, we explain the results using the most energetically unfavorable case of f_{max} (*i.e.*, f_{max} =0 for advancing mode and f_{max} =*D/L* for receding mode). When the droplet loses volume, the differential energy ratio dE_P/dE_R is larger than 1, and hence the contact line pins if $\theta > \theta_R$. Similarly, if liquid is added, the differential energy ratio dE_P/dE_A is smaller than 1 if $\theta < \theta_A$. However, in this case, the differential energy terms are opposite in sign (liquid addition) and hence contact line pinning mode is favored for a ratio less than 1. Unlike the homogenous surface case (see Figure S2), the contact line fraction dictating the pinning is different during the advancing (f_{max} =0) and receding modes (f_{max} =*D/L*), and hence results in different de-pinning angles leading to the contact angle hysteresis (Figure 4). If the contact lines do not distort and the droplet

maintains a perfectly circular shape, the magnitude of the differential energy terms during the advancing and the receding modes will be determined by the area fraction and hence will be identical. For such a case, the contact angles on a heterogeneous surface would be given by the classical CB equation. However, as shown above, hysteresis is energetically possible on a heterogeneous surface even if the individual components do not have intrinsic hysteresis.

In Fig. 5, the above analysis is presented as a generalized contact angle hysteresis regime map. The upper plots show the relationship between f_{max} and sf while the lower plots represent the corresponding trends in advancing and receding contact angles. It should be noted that most practical homogenous surface will have intrinsic contact angle hysteresis[15], and hence, the advancing and receding angles on the corresponding homogenous baseline surfaces (sf = 0 or 1) are not the same. In addition, the patterns at area fractions larger than the packing limit serve to illustrate the concept of area interconnectivity. Therefore, the trends for $sf = sf_{pack}$ towards 1 in Figure 5a are similar to the trends for $sf = sf_{pack}$ towards 0 in Figure 5b, and vice versa. Note that the definition of area fraction sf in this study is based on discrete defects and hence is different for Figures 5a and 5b.

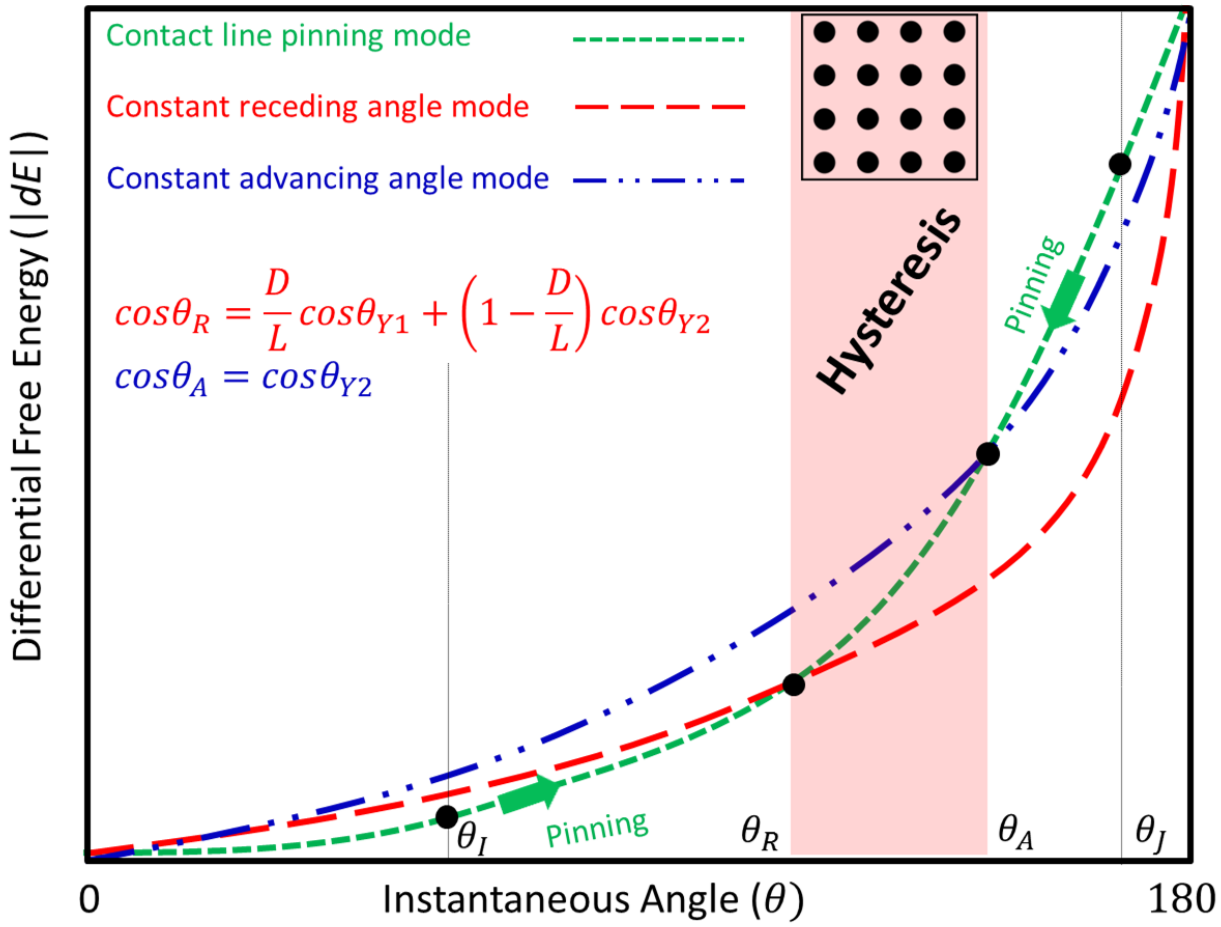

Figure 4. A representative schematic graph showing the relative magnitudes of the differential free energy terms of the contact line pinning, constant receding angle, and advancing angle modes for the most energetically unfavorable case of f_{max}. The sign of the differential energy terms are opposite for the cases of volume addition and loss. If liquid is removed from a droplet with contact angle θ_J, $dE_P/dE_R > 1$, droplet is pinned and the contact angle decreases (short-dash green line with a backward arrow) until θ_R, where $dE_P/dE_R = 1$, allowing the droplet to adopt a receding mode with a constant contact angle θ_R. Conversely, if liquid is added to a droplet and the contact angle is θ_I in which case $dE_P/dE_A < 1$, droplet is pinned and the contact angle increases (short-dash green line with a forward arrow) until θ_A, when $dE_P/dE_A = 1$, allowing the droplet to adopt an advancing mode with a constant contact angle θ_A.

The regime map for a heterogeneous surface with hydrophilic defects is summarized in Figure 5a. As discussed in the above analysis, at $sf = f_{max} = 0$, the advancing and receding contact angles correspond to that on area "2", while at $sf = f_{max} = 1$ the angles correspond to area "1". As the area fraction of the pattern is varied from 0 to the packing limit ($sf = 0.79$), the fraction of the contact line (f_{max}) on these defects during the receding mode varies from 0 to 1 (Figure 5a, top). The receding contact angle in this case can then be modeled using the corresponding receding contact angle values of the baselines as follows:

$$\cos\theta_R = f_{max}\cos\theta_{1,R} + (1 - f_{max})\cos\theta_{2,R} \quad (7)$$

where $f_{max} = D/L$ for circular hydrophilic defects. Equation 7 is similar to Eq. 5 with a small modification to include intrinsic contact angle hysteresis, *i.e.*, θ_{Y1} and θ_{Y2} in Eq. 5 are replaced by $\theta_{1,R}$ and $\theta_{2,R}$ in Eq. 7, respectively. The thermodynamically allowable fraction of the contact line (f_{max}) on these defects during the advancing mode is 0 and hence the advancing contact angle remains constant ($\cos\theta_A = \cos\theta_{2,A}$) so long as the domain "2" is interconnected.

Once the packing limit is reached, the interconnectivity of the domain "2" is lost and the more hydrophilic domain "1" becomes interconnected. Under such a situation where the area fraction of the hydrophilic domain varies from the packing limit to 1, the advancing contact varies from the value corresponding to domain "2" to that on domain "1". The receding contact angle is constant and corresponds to domain "1". Similar to Eq. 7, an equivalent expression can be derived for the advancing contact angle if the shapes on the isolated hydrophilic defects are known. This situation, however, is qualitatively similar to Figure 5b where the interconnected area is hydrophilic. For such a case, the advancing contact can be modeled using an expression equivalent to Eq. 7 as follows:

$$\cos\theta_A = f_{max}\cos\theta_{1,A} + (1 - f_{max})\cos\theta_{2,A}, \quad (8)$$

where $f_{max} = D/L$ for circular hydrophobic defects. The fraction of the contact line (f_{max}) on these defects during the receding mode is 0 and hence the receding contact angle remains constant ($\cos\theta_R = \cos\theta_{1,R}$) as long as the hydrophilic domain "1" is interconnected.

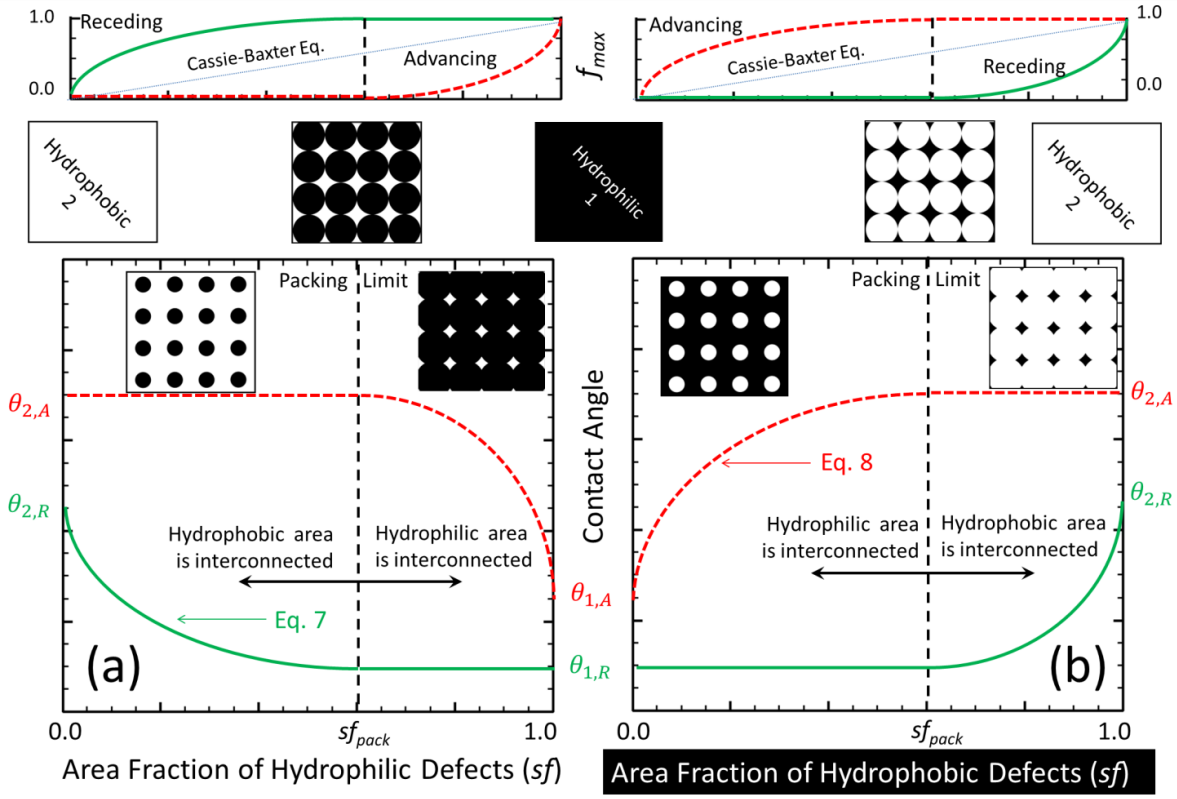

Figure 5. A schematic representation of the contact angle hysteresis regimes for a heterogeneous surface where the square array of circular defects is relatively (a) hydrophilic, and (b) hydrophobic. The variation of the fraction of contact line (f_{max}) is shown in the top plots while the corresponding advancing and receding contact angles are shown in the bottom plots. The dashed-red lines correspond to advancing phase while the solid-green lines represent the receding phase. Note that the "hydrophilicity" and "hydrophobicity" of the baseline surfaces in these schematics are relative and do not strictly imply a contact angle smaller or larger than 90°.

The proposition where the advancing contact angle for surfaces with hydrophilic defects is constant (Figure 5a, $0 \leq sf \leq 0.79$), corresponds to the observations of Li *et al.*[16], who reported that for the case of a high contact angle (low energy) solid surface with more wetting (higher energy) impurities/defects, the advancing contact angles were more reproducible than the receding contact angles. The advancing contact angles were suggested to be representative of the actual energy of the thin-film coated surface, while the receding contact angle was shown to be linked to defects/impurities in the thin-film coating, and was hence suggested to be disregarded when the main goal was the characterization of the thin film energetics. Similar observations have also been reported for CB droplets (heterogeneous surface of pillar tops and air) on superhydrophobic surfaces where the advancing angle has been reported to be independent of solid fractions[8f, g, 8k, 8m]. Ideally, the advancing angle in such cases should be 180^o corresponding to the surrounding vapor/gas phase, but is difficult to attain in practical experiments due to gravitational effects[8k].

3. Experiments with Patterned Heterogeneous Surfaces

Dynamic contact angle measurements were performed at room temperature (22-25°C) and a relative humidity of 33-45%. An automatic microscopic contact angle meter (MCA-3, Kyowa Interface Science) was used for the experiments. Reagent grade water (Sigma-Aldrich, CAS no. 7732-18-5) was used as the fluid. A piezo ink jet (PIJ) head dispensed ultra-small droplets with a volume of ~15 picoliters at a rate of 40-50 Hz for ~20 to 35 seconds allowing ample time to monitor the advancing contact angle. There was negligible influence of the PIJ dispensing frequency on contact angle behavior which was confirmed from measurements showing a constant advancing contact angle value for liquid addition rates ranging from 0.15 nL/sec at 10 Hz to 3.0 nL/sec at 200 Hz. Once a sufficiently large droplet (~ 20 nL) was formed, the PIJ was turned off and the droplet was monitored while evaporating. Side view and top view images of the droplet

were acquired at 10 Hz. Due to the placement of the PIJ during the droplet advancing phase, top view images could only be acquired during evaporation (pinning and receding phases). Embedded image processing software (FAMAS) used the half-angle method to determine the contact angle with a high resolution of 0.1° from the side view images. The half-angle method calculates the contact angle θ from the angle φ between the droplet base line and the line passing beyond the apex of the droplet based on the assumption that the droplet is small (maximum droplet volume in this study is less than 25 nL) and forms a spherical cap. The contact angles were repeatable to within ±2° and the uncertainty in measurements was within ±1°.

Heterogeneous test samples were designed for systematic contact angle hysteresis experiments with controlled defects on the order of 10 μm as shown in Figure 6. To fabricate these surfaces, photoresist (~1 μm) was spin coated at 3000 rpm for 30 s on a thermally oxidized, un-doped silicon wafer (SiO_2 thickness ~ 300 nm). The heterogeneous area of the samples were defined by a photolithography mask of circular arrays with diameters of 3 and 4 μm and center-to-center spacings of 6, 8, and 16 μm. To obtain samples with inverse patterns one wafer was spin-coated with a positive photoresist (OCG 825, Arch Chemicals) while the second wafer was coated with a negative photoresist (AZ 5214, Clariant Corporation) (see the bottom of Figure 6a). Spin coating was sequentially followed by a soft bake, UV exposure, photoresist development, and post bake resulting in samples as shown in Figure 6a on the left-hand side. The thickness of the photoresist layer after baking and exposure to oxygen plasma for 2 minutes was ~ 0.7-0.9 μm resulting in a maximum roughness of $r_{max} = 1.08$ for the heterogeneous area.

In order to isolate the effect of chemical heterogeneity, a set of the photoresist based samples were post-processed to obtain an optically smooth heterogeneous surface (Figure 6b) comprised of a hydrophobic silane coating and SiO_2. Dichlorodimethylsilane (Sigma-Aldrich), a

short chain silane with a low contact angle hysteresis ($\theta_A = 102° \pm 1.5°,\ \theta_R = 99° \pm 1.5°, \Delta\theta = 3° \pm 2°$), was deposited using chemical vapor deposition (CVD) onto the exposed SiO_2 regions of the photoresist-coated samples. The covalently bonded thin-film had a RMS roughness of 3.8 nm as measured by atomic force microscopy corresponding to a maximum roughness ratio r_{max} of 1.002. The samples were then sonicated in acetone (Macron, Chemicals, CAS no. 67-64-1) to lift-off the remaining photoresist (no effect on silane bonded to SiO_2), exposing the underlying SiO_2 surface.

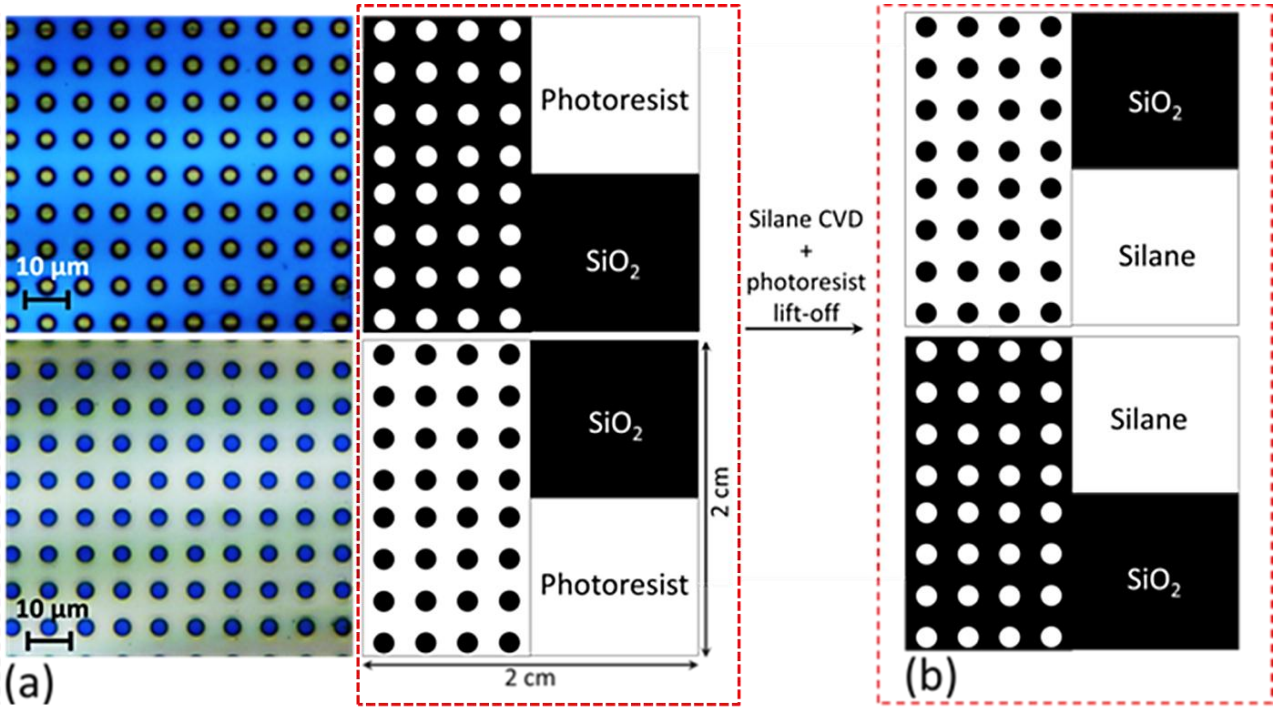

Figure 6. (a) Color optical images of the patterned areas (sample number 5 on top left and sample number 11 on bottom left). Also shown on the right are the schematics of the corresponding test samples with three test areas: (1) Photoresist, (2) SiO_2, and (3) Pattern. (b) Schematic of the corresponding silane based samples obtained after CVD and photoresist lift-off.

Contamination is an important issue in surface wettability studies and can often be overlooked, *e.g.,* the controversy in the earlier literature concerning the surface energy of gold[17]. Here, we paid special attention in the experiments to rule out effects of the test fluid and surface contamination. As mentioned previously, reagent grade water was used as the test fluid and the absence of any observable residue after complete droplet evaporation indicated that there was minimal contamination from the test fluid. The test surfaces were also thoroughly cleaned (section S2 of the supplementary information contains the details of cleaning procedures), but the intrinsic wettability of a surface can evolve due to the adsorption of different chemical groups from ambient as time passes[18]. To mitigate errors associated with surface contamination following cleaning and the variation in waiting time between measurements, the mask was designed such that, after the fabrication process (Figure 6a right), a 1x1 cm^2 spot on each sample (2x2 cm^2) was left coated with either photoresist or silane (baseline) while another 1x1 cm^2 spot was left bare (SiO_2 baseline). The remaining 1x2 cm^2 rectangular area was patterned with regions of SiO_2 and photoresist or silane, which served as the heterogeneous surface for model validation during *in-situ* measurements of the three surface regions. Table 1 shows the test matrix with the details of 12 photoresist-based and 12 silane-based samples. Two sets of experiments were performed on the photoresist-based surfaces (sample number 1-12) to investigate the influence of cleaning methodologies (section S2 of the supplementary information).

Table 1. Test matrix of patterned samples. Note that the definition of "*sf*" and "*f*" are based on the discrete defects. As a result, for sample numbers 1-6, *sf* corresponds to the area fraction of photoresist, while for sample numbers 7-12, *sf* corresponds to the area fraction of SiO_2. The last column identifies the sample with respect to the two regimes discussed in Figure 5.

Sample no.	D (μm)	L (μm)	Patterned Area	Interconnected Area	*sf*	Case
1 (13)[a]	3	6	Photoresist (SiO_2)	SiO_2 (silane)	0.20	Figure 5b (5a)
2 (14)	3	8	Photoresist (SiO_2)	SiO_2 (silane)	0.11	Figure 5b (5a)
3 (15)	3	16	Photoresist (SiO_2)	SiO_2 (silane)	0.03	Figure 5b (5a)
4 (16)	4	6	Photoresist (SiO_2)	SiO_2 (silane)	0.35	Figure 5b (5a)
5 (17)	4	8	Photoresist (SiO_2)	SiO_2 (silane)	0.20	Figure 5b (5a)
6 (18)	4	16	Photoresist (SiO_2)	SiO_2 (silane)	0.05	Figure 5b (5a)
7 (19)	3	6	SiO_2 (silane)	Photoresist (SiO_2)	0.20	Figure 5a (5b)
8 20)	3	8	SiO_2 (silane)	Photoresist (SiO_2)	0.11	Figure 5a (5b)
9 (21)	3	16	SiO_2 (silane)	Photoresist (SiO_2)	0.03	Figure 5a (5b)
10 (22)	4	6	SiO_2 (silane)	Photoresist (SiO_2)	0.35	Figure 5a (5b)
11 (23)	4	8	SiO_2 (silane)	Photoresist (SiO_2)	0.20	Figure 5a (5b)
12 (24)	4	16	SiO_2 (silane)	Photoresist (SiO_2)	0.05	Figure 5a (5b)

[a]The respective information for the silane based samples is shown in the parentheses.

4. Experimental Results and Validation

(a) Experimental results on photoresist-based heterogeneous surfaces

A sample experiment for sample number 4 and run number 2 is shown on Figure 7a. The contact angle quickly approached a constant value during the liquid addition phase (constant advancing angle mode). The figure shows that the advancing contact angle on the patterned area was between the measured values for the two baseline surfaces. Once liquid addition was stopped, the contact angle decreased due to evaporation while the contact line remained pinned. The receding contact

angle for all three surfaces was small (~ 2-6°) and differences between them were comparable to the uncertainty in the measurements (~ ±1°). Nonetheless, the contact angle on the patterned area was between the receding contact angle of the SiO_2 surface and that on the photoresist. This sample represents the case where the relative wettability of the two surfaces reverses between advancing and receding modes, *i.e.*, the photoresist is less wetting during the advancing mode while SiO_2 is less wetting during the receding mode. As a result, the contact line during the receding mode was distorted around the hydrophilic photoresist spots as shown on Figure 2 (sample number 6).

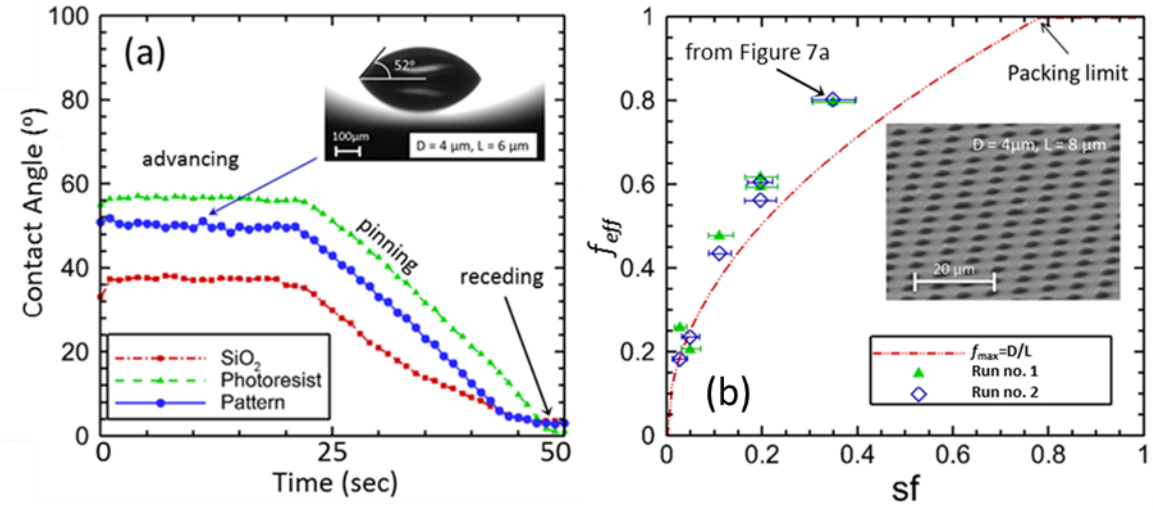

Figure 7. (a) A sample measurement result on the two respective baseline surfaces and the corresponding patterned surface (sample number 4 and run number 2). The inset shows the side view image of the droplet of volume ~ 16 nL on the patterned area at 22 seconds. (b) A comparison between the model and the experimental data for the advancing mode. The f_{eff} calculated using Eq. 9 and advancing contact angle values in (a) is highlighted as an example. A SEM image of sample number 5 is shown in the inset. The dots that appear in the form of spherical caps are the photoresist coating.

The advancing contact angle measurement results for sample numbers 1-6 and the two different cleaning procedures are shown on Table 2. The baseline contact angles were found to evolve due to the cleaning methodology and varied considerably between the samples. Nonetheless, the time gap between the three measurements on any one sample (two on baseline surfaces and one on pattern) was less than five minute such that that significant changes in the surface energy (with exposure to ambient) during experiments were negligible. The advancing angles on samples 1-6 are similar to the situation discussed in Figure 5b where the relatively hydrophilic area (SiO_2 in the current case) is interconnected and hence the advancing angle is based on the f_{max} as defined in Eq. 8. To validate this behavior, the effective f (based on the respective baseline advancing contact angle values) that would result in the observed contact angle on the patterned surface was calculated for the two runs as follows:

$$f_{eff,A} = (\cos\theta_{pattern,A} - \cos\theta_{SiO_2,A})/(\cos\theta_{photoR,A} - \cos\theta_{SiO_2,A}) \quad (9)$$

Table 2. Advancing contact angle measurement results on sample numbers 1-6. Run number 1 and run number 2 correspond to the different cleaning procedure discussed in the supplementary information.

Sample no.	*sf*	θ_A, run no. 1			f_{eff}	θ_A, run no. 2			f_{eff}
		SiO_2	Photoresist	Pattern		SiO_2	Photoresist	Pattern	
1	0.20	32°	44°	40°	0.60	38°	57°	50°	0.60
2	0.11	20°	45°	34°	0.48	30°	51°	40°	0.43
3	0.03	26°	56°	35°	0.24	33°	58°	39°	0.19
4[b]	0.35	32°	53°	50°	0.80	36°	56°	53°	0.80
5	0.20	21°	53°	43°	0.61	37°	57°	49°	0.57
6	0.05	28°	53°	35°	0.22	34°	57°	41°	0.26

[b]The data for run number 2 is shown in Figure 7a.

Despite the variability in the baseline contact angle values, not only was the effective f repeatable between the two runs (Table 2, Figure 7b), but also followed the trend as predicted by Eq. 8. Slight discrepancies (RMS_{error} in f_{max} was 0.07) between the experimental results and model predictions at higher area fractions are due to the effect of the roughness due to the photoresist layer thickness (inset of Figure 7b), and will be supported in the subsequent section with measurements on smooth silane coated surfaces. As mentioned previously, any calculations of f_{eff} with receding contact angle values were difficult to obtain due to the comparable experimental uncertainties.

The measurement results for sample numbers 7-12 (inverse pattern, Figure 6a, bottom) during the advancing phase are shown on Table 3, where the relatively non-wetting area (photoresist in the current case) was interconnected similar to the situation discussed in Figure 5a (see section S2 of supplementary information for cleaning procedure for these samples). The advancing contact angle values on the patterned area were very similar to that on the photoresist baseline, which agrees with the scenario in Figure 5a where $f_{eff} = f_{max} = 0$. The receding contact angles in this case were again very small for the baselines as well as the pattern and hence no conclusive observation could be made. Nonetheless, both of the advancing angle cases where in the first, the relatively hydrophilic area (SiO_2) was interconnected, while in the second, the relatively hydrophobic area (photoresist) was interconnected, validate the model over the complete range of area fractions, below and above the packing limit (Figure 7b). Moreover, the good agreement between the data and the model suggests the need to apply the CB equation temporally such that the effect of contact line distortion is captured. The usefulness of the *in-situ* baseline contact angle calibration for samples highly sensitive to cleaning procedure and time of exposure to ambient is also demonstrated through these results.

Table 3. Advancing contact angle measurement results on sample numbers 7-12.

Sample no.	*sf*	θ_A, run no. 1			f_{eff}	θ_A, run no. 2			f_{eff}
		SiO_2	Photoresist	Pattern		SiO_2	Photoresist	Pattern	
7	0.20	31 ^{o}	42 ^{o}	41 ^{o}	~0	26^o	31^o	31^o	~0
8	0.11	27 ^{o}	47 ^{o}	47 ^{o}	~0	25^o	33^o	34^o	~0
9	0.03	21 ^{o}	45 ^{o}	46 ^{o}	~0	25^o	34 ^{o}	34^o	~0
10	0.35	33^o	53 ^{o}	53 ^{o}	~0	26^o	34^o	33^o	~0
11	0.20	26 ^{o}	48 ^{o}	49 ^{o}	~0	25^o	33^o	32^o	~0
12	0.05	32 ^{o}	51 ^{o}	50 ^{o}	~0	24^o	34^o	34^o	~0

(b) Experiments on silane-based heterogeneous surfaces

The advancing and receding contact angle measurements on the silane-based samples are shown in Table 4 (see section S2 of the supplementary information for cleaning procedure). The relative wettability of the homogenous baseline surfaces for these samples was the same for both the advancing and the receding modes. The results for sample numbers 13-18 are similar to the scenario discussed in Figure 5a and hence the receding contact angle on the patterned surface varied with *sf* and f_{eff} was calculated using Eq. 7. The advancing contact angles on the patterned area were similar (within ±1^o) to that on the silane baseline, which is in complete agreement with $f_{eff} = f_{max} = 0$. Similarly, for the sample numbers 19-24 (Figure 5b), the receding contact angle was constant (100^o ±2^o) while the advancing contact angle was modeled using Eq. 8. The experimentally observed variation of f_{eff} with *sf* based on receding contact angle for sample number 13-18 and that based on advancing contact angle for sample numbers 19-24 are shown in Figure 8 with the model prediction f_{max}. The good agreement between the data and model confirms the validity of the model over a wide range of area fractions and also supports the conclusion that the increased deviation at higher area fractions for the photoresist-based samples in Figure 7b was a result of the non-negligible roughness of the photoresist layer.

Table 4. Advancing and receding contact angle measurement results on sample numbers 13-24.

Sample no.	*sf*	θ_A			f_{eff}	θ_R			f_{eff}
		Silane	Photoresist	Pattern		Silane	Photoresist	Pattern	
13	0.20	103 º	74 º	103 º	~0	100 º	29 º	71 º	0.48
14	0.11	103 º	77 º	102 º	~0	98 º	25 º	78 º	0.33
15	0.03	103º	78 º	103 º	~0	100 º	27 º	91 º	0.15
16	0.35	103 º	80 º	103 º	~0	101 º	33 º	63 º	0.64
17	0.20	102º	73 º	104 º	~0	97 º	35 º	74 º	0.43
18	0.05	104 º	75 º	103 º	~0	101 º	24 º	89 º	0.19
19	0.20	103 º	74 º	87 º	0.45	98 º	37 º	35 º	~0
20	0.11	103 º	73 º	83 º	0.33	100 º	39 º	37 º	~0
21	0.03	103º	77 º	82 º	0.18	101 º	35 º	34 º	~0
22	0.35	101 º	72 º	93 º	0.72	99 º	34 º	35 º	~0
23	0.20	103º	76 º	88 º	0.44	100 º	35 º	36 º	~0
24	0.05	102 º	70 º	77 º	0.21	101 º	40 º	37º	~0

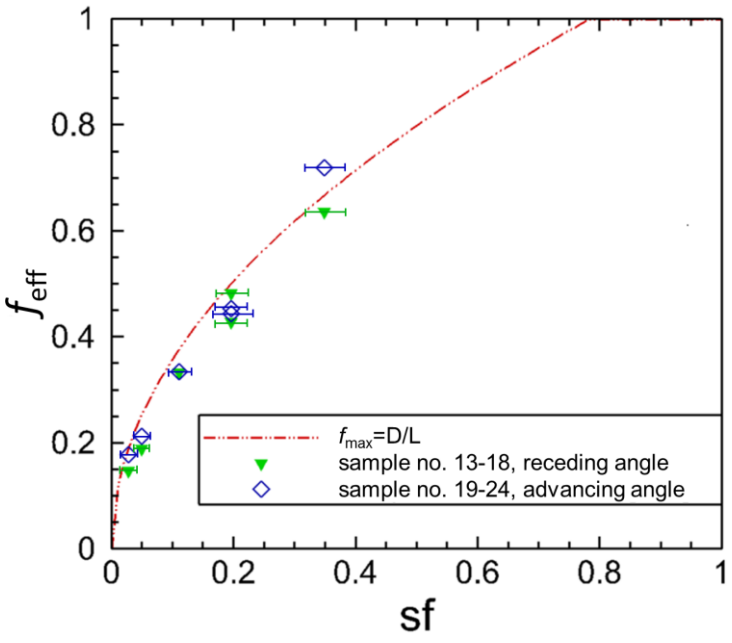

Figure 8. A comparison between the model and the experimental data for silane-based samples with various area fractions *sf*. In samples numbers 13-18, the hydrophobic silane coating is interconnected, while in samples numbers 19-24, the hydrophilic SiO_2 is interconnected.

The results of sample numbers 7-18 show that the advancing contact angle was constant and depended only on the interconnected hydrophobic area and support the conclusion that the advancing contact angle on a heterogeneous surface can be used to characterize the surface energy of the interconnected area as proposed by Li *et al.*[16]. Conversely, the current study also suggests that for the opposite case of a high energy surface with low energy defects and zero intrinsic contact angle hysteresis, the receding contact angle can be used to characterize the surface energy.

5. Modeling of Droplet Shape Evolution

Now that we showed that the presented thermodynamic model well-captures the contact line dynamics, in this section we demonstrate how this model can be used to predict the droplet shape evolution from deposition to complete evaporation. As an example, we obtained the droplet contact angle, base radius, height, and volume from experiments on the patterned area of sample number 16 as shown in Figure 9. The droplet quickly approached the advancing contact angle which is consistent with that on interconnected silane-coated region of the patterned surface ($\theta_{pattern}$~103^o). The droplet then advanced with almost constant contact angle until t = 32 s when liquid addition from PIJ was stopped. The advancing mode was then followed by a contact line pinning mode (t = 32-64 s) where the base radius remained constant and volume loss due to evaporation was accommodated by a decrease in the droplet height, resulting in a decrease in the apparent contact angle. At t = 64 s, the contact angle of the droplet was equal to that determined by $f_{\max}$ and hence the droplet began receding without any further change in contact angle, except at the very end of its life which is attributed to the fact that the droplet was very small, and hence not in a quasi-steady state.

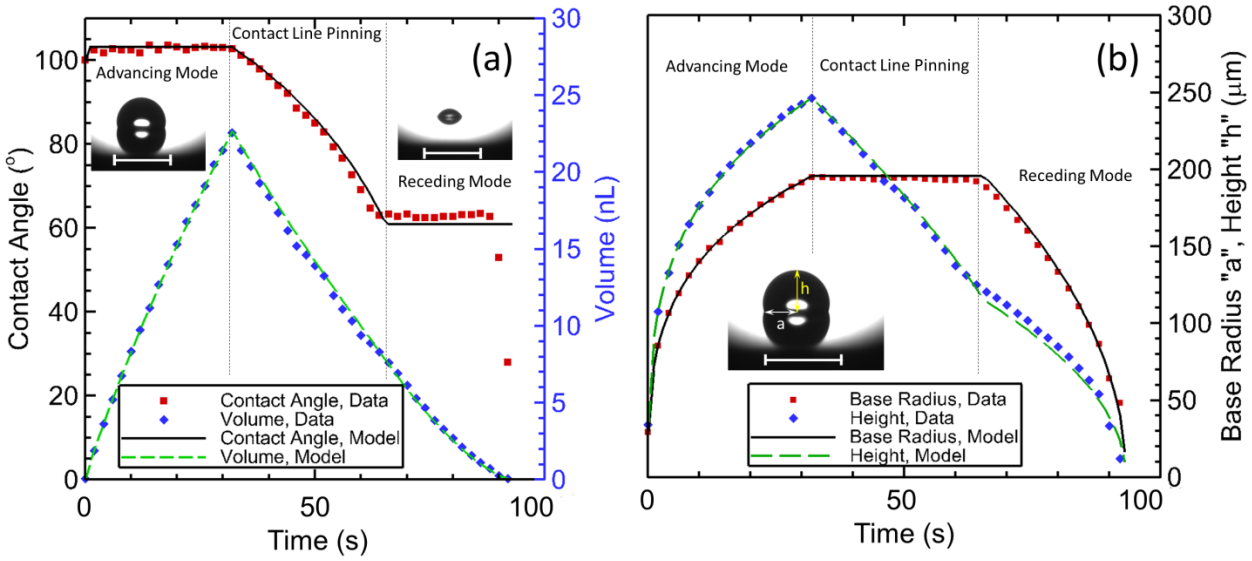

Figure 9. Comparison between the experimental results and model predictions of (a) contact angle, volume, (b) base radius, and height of the evolution of a water droplet on a heterogeneous surface. Scale bars in droplet images correspond to 500 μm.

To model the different stages of the evaporating droplet, we assumed that the time scales required for recirculation inside the droplet were much smaller than the time scales associated with droplet dynamics at the contact line. The classical model of Bourges-Monnier and Shanahan[14a] for evaporation of a sessile droplet on a substrate was used to quantify the volume loss with evaporation (see supplementary section S3, Eq. S24). The shape and area fraction of defects, baseline contact angles on the respective homogeneous surfaces, initial droplet geometry (first experimental data point), liquid addition rate, vapor diffusivity (2.6×10^{-5} m^2/sec at 25°C), and the relative humidity (RH = 38% ± 2% for results in Figure 9) of the ambient were the only defined inputs into the model. The details of the thermodynamic argument required for modeling the droplet evolution are based on the concept proposed in section 2 and are discussed in section S3 of the supplementary information.

The experiments and model predictions in Figure 9 show good agreement. The evaporation model of Bourges-Monnier and Shanahan[14a] coupled with the contact angle at any time allows accurate prediction of the experimentally observed evaporation rate (Figure 9, left). At later stages of droplet evaporation, there is a deviation between the contact angle data and the model which is attributed to the fact that for very small droplets, the time scales associated with the rate of liquid loss becomes comparable to the rate of fluid recirculation resulting in the quasi-steady assumption to be no longer valid. Hence, a mixed mode for evaporation where both the contact angle and the base radius change was adopted. Importantly, while droplet evaporation models in literature[14a-14d] can predict the time for a droplet to evaporate completely, unlike the proposed model, they cannot prescribe the fraction of times spent individually in the pinning and the receding modes, which is useful information for tailoring applications that rely on the evaporation of liquids[11-12]. Additionally, the knowledge of contact line pinning time is also essential to develop guidelines for performing contact angle hysteresis measurements (refer to the supplementary section S4 for a discussion on the effect of droplet volume on contact line pinning time).

6. Cassie-Baxter Droplets on Structured Surfaces

Having validated the model for contact angle hysteresis on nearly smooth heterogeneous surfaces, we now demonstrate the robustness of the model by predicting the contact angle hysteresis and droplet shape evolution for CB droplet data from literature. A CB droplet is, in principle similar to a case of a droplet on a heterogeneous surface where the interconnected area is a gas ($\theta = 180°$) while the functionalized "silicon pillar tops" act as relatively more hydrophilic circular defects. The experimental hysteresis data and theoretical model of Reyssat and Quéré[8k] for CB droplets on cylindrical pillar arrays is shown on Figure 10. The ordinate represents the difference of cosines

of the receding and advancing contact angles. The model was stated to be valid for well-defined strong (pinning) but dilute defects.

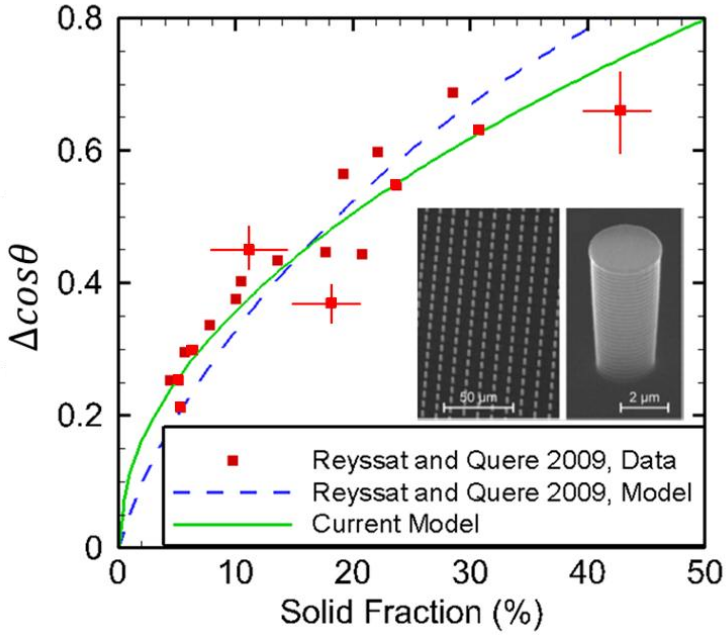

Figure 10. Comparison between the prediction of proposed model and the hysteresis data and model of Reyssat and Quéré[8k] for CB droplets on cylindrical pillar arrays (inset). The droplet volume varied between 10-20 µL and the data set contains points obtained by tilting the sample as well as by using a syringe to add/withdraw the liquid.

The case of a CB droplet on a structured surface is similar to the situation shown in Figure 5a and hence the receding contact angle from our model was calculated using Eq. 7. In comparison to the model of Reyssat and Quéré[8k], our model predicts larger hysteresis at low solid fractions ($sf < 0.15$) and smaller hysteresis at high solid fractions ($sf > 0.15$) implying an increased convexity in the hysteresis curve, which is a trend also apparent from their experimental data in Figure 10. In order to address the complexities at the contact line, Reyssat and Quéré[8k] incorporated a fitting parameter "*a*" that was said to capture the details of the contact line with an assumption that the

pillars are dilute such that each defect independently distorts the contact line. The model was specified to be valid only up to a critical solid fraction/defect density of 40% after which it was suggested that the contact lines would take "shortcuts" across the denser pillars not allowing the distortions to be independent anymore. Using our thermodynamic approach including the effect of the contact line distortion, these previous assumptions can be relaxed such that the presented model can capture the dynamics over the complete range of area fractions. Moreover, good agreement between the current predictions and the experimental data in Figure 10 which are comprised of points that were acquired both by tilting the sample as well as by supplying/withdrawing the liquid using a syringe demonstrates the robustness of the proposed model in predicting hysteresis for other widely used liquid addition/removal techniques as well.

Furthermore, we investigated the applicability of our model to capture the dynamics of an evaporating CB droplet. McHale *et al.*[14b] experimentally investigated the evaporation of a CB droplet on a patterned polymer surface (square array of cylindrical SU-8 pillars, Figure 11). As discussed for the full life simulation of droplets on the silane-based samples, the only inputs required by the proposed model were the droplet initial conditions (contact angle and base radius), the geometry of the heterogeneous surface (solid fraction), relative humidity, temperature, and the intrinsic contact angles on the baseline surface (flat surface for structures). The details as reported by McHale *et al.*[14b] are given in Figure 11. Since a range of relative humidity and temperature was reported, we have used the average values (51.5% *RH* and 24.5°C temperature) for simulations. Moreover, advancing and receding contact angles on the corresponding flat surface were not detailed and instead the reported static contact angle was used. In Figure 11, we see the prediction from the proposed model well-matches the experimental data of McHale *et al.*[14b] where the contact line pinning time and the receding contact angle show good agreement. The trend in the droplet

height and base radius during evaporation was also captured. Again, there are some discrepancies between the data and the model at the end of the droplet life when the droplet adopts the mixed evaporation mode. The agreement is encouraging despite the fact that exact conditions were not known (*RH* and receding contact angle) and average values based on the numbers prescribed in the paper were used.

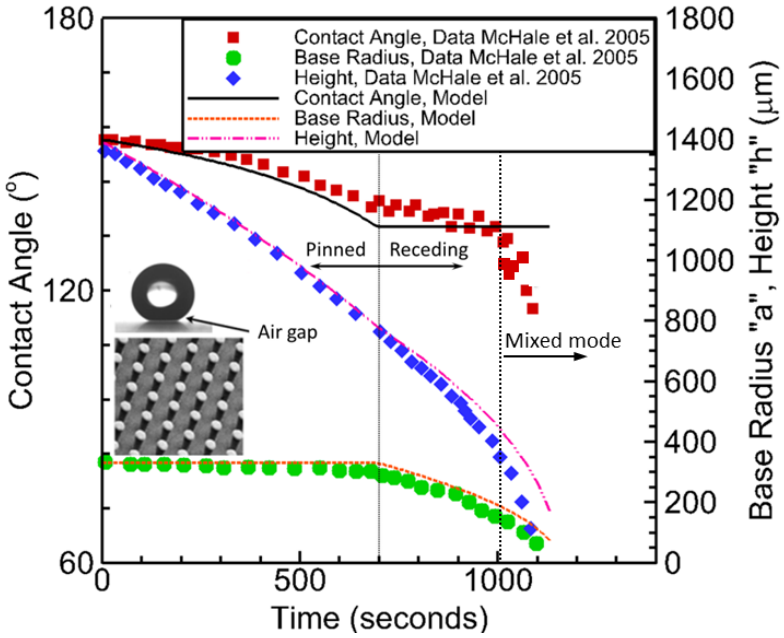

Figure 11. Comparison between the droplet evaporation data on superhydrophobic surface (inset) from McHale *et al.*[14b] and the predictions from the proposed model. Sample dimensions: D = 8 μm, L = 30 μm, H = 15 μm. Test conditions: θ_{flat}= 80°, RH = 45-58%, and $T = 23 - 26$ ℃.

The examples described above demonstrate the effectiveness of the proposed model in predicting contact angle hysteresis as well as droplet evolution throughout its lifetime on heterogeneous surfaces composed of circular defect domains. The validity of the model for photoresist and silane-based samples along with the case of CB droplets on superhydrophobic surfaces show the robustness of the proposed model over a large range of baseline contact angle values ($2° < \theta_{baseline} < 104°$). Moreover, the range of droplet volumes (maximum volume after

the end of advancing mode or after initial droplet deposition) investigated in this study was between 16 nL to 20 μL, which suggests that the current model has practical applications involving droplet manipulation. Studies with other defect shapes and their inverse patterns can be performed accordingly to develop similar predictive relations.

7. Conclusions

Geometric modeling of the contact line distortion due to pinning was adopted to develop a thermodynamic model for contact angle hysteresis on heterogeneous surfaces. *In-situ* contact angle calibrations of the constituent homogenous surfaces were shown to eliminate discrepancies due to the changes in surface wetting characteristics arising, for example, from variability in cleaning procedures or contamination from the ambient. Interconnectivity of the surfaces comprising the heterogeneous surface was shown to play a key role in the contact line dynamics. For a low energy surface with high energy defects, the advancing contact angle was independent of the defect fraction and matched the corresponding value on the homogenous low energy surface. The receding contact angle, on the other hand, was shown to be influenced by the contact line distortion and depended on the relative fraction of the contact line on the respective surfaces. The fraction of the contact line on each surface was modeled and found to be a function of area fraction of the respective surfaces. The trends reversed upon the reversal of interconnectivity (high energy surface interconnected and low energy surface as defects) where the receding contact angle was found to be independent of the discrete hydrophobic defects while the advancing angle was influenced by contact line distortion. The thermodynamic model was extended to predict the droplet dynamics during the advancing, pinning and receding modes. The same model was then shown to predict the contact angle hysteresis equally well at low and high solid fractions on a superhydrophobic

surface. The experimental results reported in the paper along with the modeling effort promise to facilitate

ACKNOWLEDGMENT

The authors would like to acknowledge the support from the National Science Foundation through the Major Research Instrumentation Grant for Rapid Response Research (MRI-RAPID). R. R. acknowledges fellowship support from Battelle's National Security Global Business with Dr. Robert Carnes as the Director of Internal Research and Development Programs. R.E. acknowledges funding received from the Irish Research Council for Science, Engineering, and Technology, cofunded by Marie Curie Actions under FP7.

REFERENCES

1. Quéré, D., Wetting and roughness. *Annu. Rev. Mater. Res.* **2008,** *38*, 71-99.
2. Young, T., An Essay on the Cohesion of Fluids. *Philosophical Transactions of the Royal Society of London* **1805,** *95* (ArticleType: research-article / Full publication date: 1805 /), 65-87.
3. Wenzel, R. N., Resistance of solid surfaces to wetting by water. *Industrial & Engineering Chemistry* **1936,** *28* (8), 988-994.
4. Cassie, A. B. D.; Baxter, S., Wettability of porous surfaces. *Transactions of the Faraday Society* **1944,** *40*, 546-551.
5. (a) Anderson, D.; Davis, S., The spreading of volatile liquid droplets on heated surfaces. *Physics of Fluids* **1995,** *7*, 248; (b) Raj, R.; Kunkelmann, C.; Stephan, P.; Plawsky, J.; Kim, J., Contact line behavior for a highly wetting fluid under superheated conditions. *International Journal of Heat and Mass Transfer* **2012,** *55* (9-10), 2664-2675.
6. Gao, L.; McCarthy, T. J., How Wenzel and Cassie Were Wrong. *Langmuir* **2007,** *23* (7), 3762-3765.
7. McHale, G., Cassie and Wenzel: Were They Really So Wrong? *Langmuir* **2007,** *23* (15), 8200-8205.
8. (a) Johnson, R.; Dettre, R. H., Contact angle hysteresis. *Contact angle, wettability, and adhesion. Advances in Chemistry Series* **1964,** *43*, 112-135; (b) Dettre, R. H.; Johnson Jr, R. E., Contact Angle Hysteresis. IV. Contact Angle Measurements on Heterogeneous Surfaces1. *The journal of physical chemistry* **1965,** *69* (5), 1507-1515; (c) Johnson Jr, R. E.; Dettre, R. H., Contact angle hysteresis. III. Study of an idealized heterogeneous surface. *The journal of physical chemistry* **1964,** *68* (7), 1744-1750; (d) Joanny, J.; De Gennes, P.,

A model for contact angle hysteresis. *The Journal of Chemical Physics* **1984,** *81* (1), 552-562; (e) Zhao, H.; Beysens, D., From droplet growth to film growth on a heterogeneous surface: condensation associated with a wettability gradient. *Langmuir* **1995,** *11* (2), 627-634; (f) Yeh, K. Y.; Chen, L. J.; Chang, J. Y., Contact angle hysteresis on regular pillar-like hydrophobic surfaces. *Langmuir* **2008,** *24* (1), 245-251; (g) Cho, K. H.; Chen, L. J., Fabrication of sticky and slippery superhydrophobic surfaces via spin-coating silica nanoparticles onto flat/patterned substrates. *Nanotechnology* **2011,** *22*, 445706; (h) Gao, L.; McCarthy, T. J., Contact angle hysteresis explained. *Langmuir* **2006,** *22* (14), 6234-6237; (i) Extrand, C., Model for contact angles and hysteresis on rough and ultraphobic surfaces. *Langmuir* **2002,** *18* (21), 7991-7999; (j) Extrand, C., Contact angles and hysteresis on surfaces with chemically heterogeneous islands. *Langmuir* **2003,** *19* (9), 3793-3796; (k) Reyssat, M.; Quéré, D., Contact Angle Hysteresis Generated by Strong Dilute Defects†. *The Journal of Physical Chemistry B* **2009,** *113* (12), 3906-3909; (l) Drelich, J., Static contact angles for liquids at heterogeneous rigid solid surfaces. *Polish Journal of Chemistry* **1997,** *71* (5), 525-549; (m) Choi, W.; Tuteja, A.; Mabry, J. M.; Cohen, R. E.; McKinley, G. H., A modified Cassie-Baxter relationship to explain contact angle hysteresis and anisotropy on non-wetting textured surfaces. *Journal of colloid and interface science* **2009,** *339* (1), 208-216; (n) Dorrer, C.; Rühe, J., Contact line shape on ultrahydrophobic post surfaces. *Langmuir* **2007,** *23* (6), 3179-3183; (o) Kusumaatmaja, H.; Yeomans, J., Modeling contact angle hysteresis on chemically patterned and superhydrophobic surfaces. *Langmuir* **2007,** *23* (11), 6019-6032; (p) Koishi, T.; Yasuoka, K.; Fujikawa, S.; Zeng, X. C., Measurement of Contact-Angle Hysteresis for Droplets on Nanopillared Surface and in the Cassie and Wenzel States: A Molecular Dynamics

Simulation Study. *ACS nano* **2011**; (q) Li, W.; Amirfazli, A., A thermodynamic approach for determining the contact angle hysteresis for superhydrophobic surfaces. *Journal of colloid and interface science* **2005,** *292* (1), 195-201; (r) Anantharaju, N.; Panchagnula, M. V.; Vedantam, S.; Neti, S.; Tatic-Lucic, S., Effect of three-phase contact line topology on dynamic contact angles on heterogeneous surfaces. *Langmuir* **2007,** *23* (23), 11673-11676; (s) Xu, W.; Choi, C. H., From Sticky to Slippery Droplets: Dynamics of Contact Line Depinning on Superhydrophobic Surfaces. *Physical Review Letters* **2012,** *109* (2), 024504.

9. Krumpfer, J. W.; Bian, P.; Zheng, P.; Gao, L.; McCarthy, T. J., Contact Angle Hysteresis on Superhydrophobic Surfaces: An Ionic Liquid Probe Fluid Offers Mechanistic Insight. *Langmuir* **2011**.

10. Yu, Y.; Wu, Q.; Zhang, K.; Ji, B. H., Effect of triple-phase contact line on contact angle hysteresis. *SCIENCE CHINA Physics, Mechanics & Astronomy* **2012**, 1-6.

11. Jing, J.; Reed, J.; Huang, J.; Hu, X.; Clarke, V.; Edington, J.; Housman, D.; Anantharaman, T. S.; Huff, E. J.; Mishra, B., Automated high resolution optical mapping using arrayed, fluid-fixed DNA molecules. *Proceedings of the National Academy of Sciences* **1998,** *95* (14), 8046.

12. Fan, F.; Stebe, K. J., Assembly of colloidal particles by evaporation on surfaces with patterned hydrophobicity. *Langmuir* **2004,** *20* (8), 3062-3067.

13. Kuncicky, D. M.; Velev, O. D., Surface-guided templating of particle assemblies inside drying sessile droplets. *Langmuir* **2008,** *24* (4), 1371-1380.

14. (a) Bourges-Monnier, C.; Shanahan, M., Influence of evaporation on contact angle. *Langmuir* **1995,** *11* (7), 2820-2829; (b) McHale, G.; Aqil, S.; Shirtcliffe, N.; Newton, M.;

Erbil, H., Analysis of droplet evaporation on a superhydrophobic surface. *Langmuir* **2005,** *21* (24), 11053-11060; (c) Hu, H.; Larson, R. G., Evaporation of a sessile droplet on a substrate. *The Journal of Physical Chemistry B* **2002,** *106* (6), 1334-1344; (d) Kulinich, S.; Farzaneh, M., Effect of contact angle hysteresis on water droplet evaporation from super-hydrophobic surfaces. *Applied Surface Science* **2009,** *255* (7), 4056-4060.

15. Chen, Y.; Helm, C.; Israelachvili, J., Molecular mechanisms associated with adhesion and contact angle hysteresis of monolayer surfaces. *The journal of physical chemistry* **1991,** *95* (26), 10736-10747.

16. Li, D.; Neumann, A., Surface heterogeneity and contact angle hysteresis. *Colloid & Polymer Science* **1992,** *270* (5), 498-504.

17. Schrader, M. E., Ultrahigh-vacuum techniques in the measurement of contact angles. II. Water on gold. *The journal of physical chemistry* **1970,** *74* (11), 2313-2317.

18. Takeda, S.; Fukawa, M.; Hayashi, Y.; Matsumoto, K., Surface OH group governing adsorption properties of metal oxide films. *Thin Solid Films* **1999,** *339* (1), 220-224.

Supplementary Information

S1. Thermodynamic analysis of a droplet on a homogenous surface

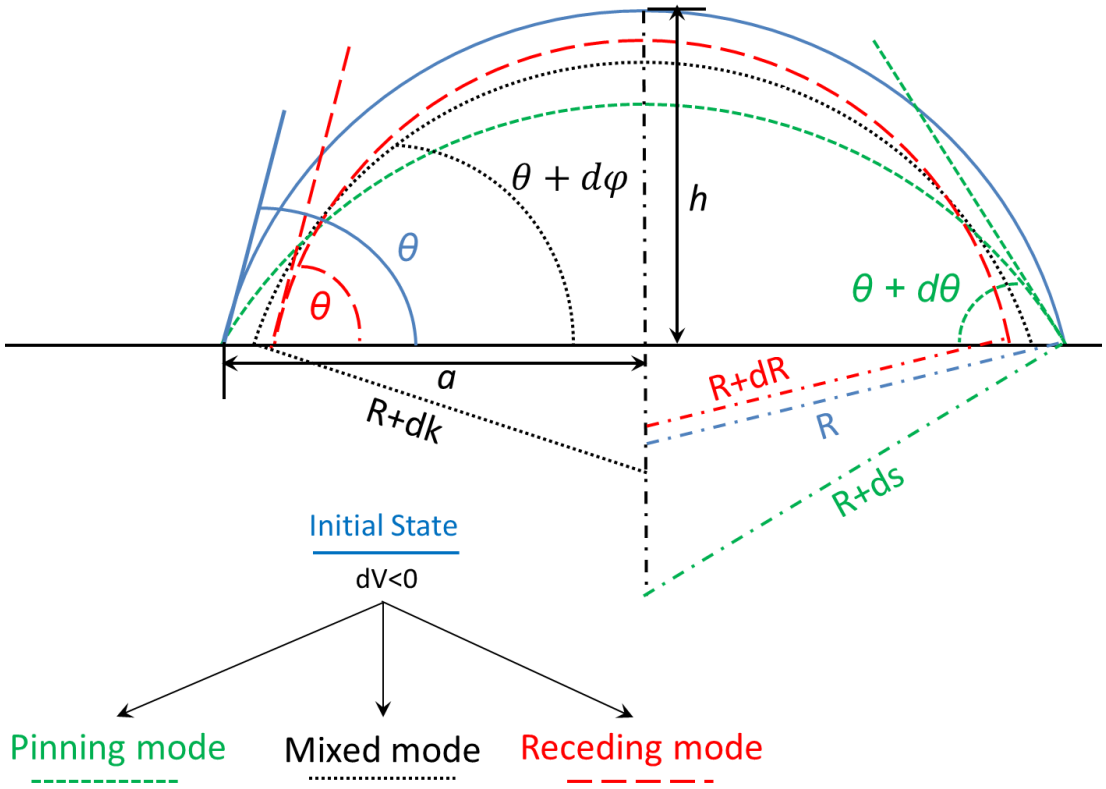

Figure S1. A schematic describing the three possibilities for a droplet (losing liquid, $dV<0$) with an initial contact angle θ and major radius R. In the contact line pinning mode, the droplet can lose volume by keeping the base radius a constant such that the contact angle decreases. In the constant receding angle mode, the droplet base radius can shrink keeping the contact angle constant. The third scenario is a mixed mode where both the contact angle as well as the base radius shrink. NOTE: To avoid confusion with the change in major radius R during the constant receding angle mode, the change in major radius R during the contact line pinning mode and mixed mode are denoted as "*ds"* and *"dk"*, respectively. Similarly, the change in the contact angle θ during the mixed mode is denoted as "$d\varphi$" in order to clearly differentiate it from that during contact line pinning mode.

Geometric Parameters:

$h = R(1 - cos\theta)$

$a = Rsin\theta$

$V = \frac{1}{3}\pi R^3(2 - 3\cos\theta + cos^3\theta)$

$A_{lv} = 2\pi R^2(1 - \cos\theta)$

$A_{sl} = \pi R^2 sin^2\theta$

Contact Line Pinning Mode

During the contact line pinning mode, the base radius is constant. As a result, a relation between the change in major radius *ds* and the change in contact angle $d\theta$ can be written as follows:

$ds = -Rcot\theta d\theta$ (S1)

The volume change is a function of two variables and hence can be calculated as follows:

$dV_P = \frac{\partial V}{\partial R}dS + \frac{\partial V}{\partial \theta}\, d\theta$

$dV_P = \pi R^2(2 - 3\cos\theta + cos^3\theta)dS + \pi R^3(sin\theta - cos^2\theta sin\theta)d\theta$

Substituting the value of *ds* from Eq. S1:

$dV_P = \pi R^3 \frac{(1-2cos\theta+cos^2\theta)}{sin\theta} d\theta$ (S2)

Similarly, the change in the spherical cap area can be calculated as follows:

$dA_{lv,P} = \frac{\partial A}{\partial R}dS + \frac{\partial A}{\partial \theta}\, d\theta$

$dA_{lv,P} = 4\pi R(1 - \cos\theta)dS + 2\pi R^2(sin\theta)d\theta$

Substituting the value of *ds* from Eq. S1:

$dA_{lv,P} = 2\pi R^2 \frac{(1-2cos\theta+cos^2\theta)}{sin\theta} d\theta$ (S3)

The change in the solid-liquid area is 0 due to contact line pinning.

$dA_{sl,P} = 0$

Hence, the change in energy due to volume loss is:

$$dE_P = \gamma_{lv}\, dA_{lv,P} = 2\,\pi R^2 \gamma_{lv}\, \frac{(1-2cos\theta+cos^2\theta)}{sin\theta} d\theta \quad \text{(S4)}$$

Constant Receding Angle Mode

During the contact receding angle mode, the volume change is only a function of major radius R as follows:

$$dV_R = \pi R^2(2 - 3\cos\theta + cos^3\theta)dR \quad \text{(S5)}$$

Similarly, the change in the spherical cap area can be calculated as follows:

$$dA_{lv,R} = 4\,\pi R(1 - cos\theta)dR \quad \text{(S6)}$$

The change in the solid-liquid area can be calculated by taking the differential of the base area as follows:

$$dA_{sl,R} = 2\,\pi R sin^2\theta dR \quad \text{(S7)}$$

Hence, the change in energy due to volume loss is:

$$dE_R = (\gamma_{sl} - \gamma_{sv})dA_{sl,R} + \gamma_{lv}\, dA_{lv,R}$$

Using Eq. S6 and S7:

$$dE_R = -2\,\pi R(\gamma_{sv} - \gamma_{sl})sin^2\theta dR + 4\,\pi R\gamma_{lv}(1 - cos\theta)dR \quad \text{(S8)}$$

Comparison

Let us first compare the contact line pinning mode and the constant receding angle mode. In order to determine which of the two modes is favored thermodynamically, a relation between dR and $d\theta$ is required. Such a relation between $d\theta$ and dR can be found by equating the differential volumes in the two modes, *i.e.* $dV_P = dV_R$.

Using Eqs. S2 and S5:

$$\frac{dR}{Rd\theta} = \left[\frac{1-2cos\theta+cos^2\theta}{sin\theta(2-3\cos\theta+cos^3\theta)}\right] \quad \text{(S9)}$$

By combining this equation with Eqs. S4 and S8, the differential energy ratio of the two modes is:

$$\frac{dE_P}{dE_R} = \left[\frac{2-3\cos\theta+cos^3\theta}{-\frac{(\gamma_{SV}-\gamma_{SL})}{\gamma_{lv}}sin^2\theta\ +2(1-cos\theta)}\right] \quad \text{(S10)}$$

Using Young's equation[2]:

$$\frac{dE_P}{dE_R} = \left[\frac{2-3\cos\theta+cos^3\theta}{-cos\theta_Y sin^2\theta\ +2(1-cos\theta)}\right] \quad \text{(S11)}$$

If the contact angle θ of the droplet is equal to the Young's contact angle for the surface:

$dE_P = dE_R$

This result implies that if the instantaneous contact angle that a droplet makes with the surface is equal to the contact angle prescribed by Young's equation, both the contact line pinning mode as well as the constant receding angle mode are equally favored.

Now, if the contact angle θ that the droplet makes with a surface with Young's contact angle θ_Y are different and can be described as follows:

$$\theta_Y\ = \theta + d\alpha \quad \text{(S12)}$$

Then,

$$\frac{dE_P}{dE_R} = \left[\frac{1}{1+\frac{sin^3\theta d\alpha}{2-3\cos\theta+cos^3\theta}}\right] \quad \text{(S13)}$$

NOTE: $d\alpha$ is used here to describe the change in contact angle θ in order to differentiate it from $d\theta$ used previously (Eqs. S1-S11) which represents the change in contact angle with volume change. On the other hand, $d\alpha$ represents the difference between the Young's contact angle θ_Y and the actual contact angle θ that the droplet makes with the surface at any instant.

If $d\alpha$<0, *i.e.* $\theta_Y < \theta$ as shown on Figure S2,

$\frac{dE_P}{dE_R} > 1$

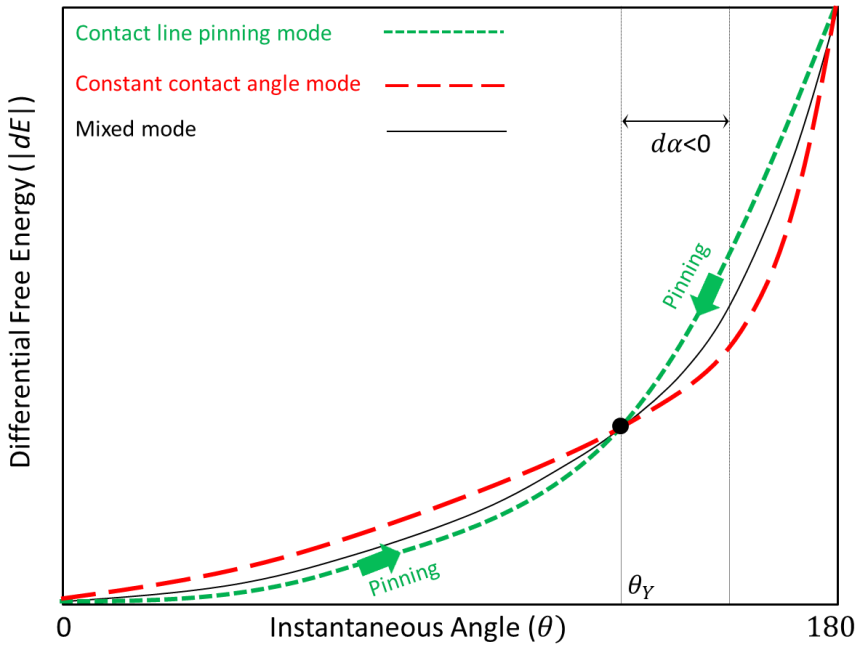

Figure S2. A representative schematic graph showing the relative magnitudes of the differential free energy terms of the contact line pinning, constant receding angle mode, constant advancing angle mode, and mixed mode for a homogenous surface. The sign of the differential energy terms are opposite for the cases of volume addition and loss.

In this case, the contact line pinning mode is preferred and the droplet would prefer to lose volume with contact line being pinned and a continuous decrease in contact angle until $\theta_Y = \theta$ is satisfied. At $\theta_Y = \theta$, both modes are equally favored. The droplet can also lose volume in the constant receding contact angle mode henceforward. However, if the contact line continues to be pinned such that the contact angle gets differentially smaller ($|d\alpha| \to 0$) than the Young's contact angle such that:

If $\theta_Y > \theta$, *i.e.* $d\alpha$>0

$\frac{dE_P}{dE_R} < 1$

then the constant receding angle mode will be favored with the contact angle essentially being the Young's contact angle ($\theta_Y \ = \theta + d\alpha, and\ |d\alpha| \to 0\ implying\ \theta_Y \sim \theta$).

Similar analysis is also valid when liquid is added to the droplet. In such a case, the droplet can adjust for the additional volume either by keeping the base radius *a* constant (contact line pinning mode) and increasing the contact angle, or by keeping the contact angle constant (constant advancing angle mode) where the base radius would be required to increase.

$$\frac{dE_P}{dE_A} = \left[\frac{1}{1+\frac{sin^3\theta d\alpha}{2-3\cos\theta+cos^3\theta}}\right] \tag{S14}$$

where the subscript A represents constant advancing angle mode as a result of volume addition.

Again, if $\theta_Y \ > \theta$, *i.e.* $d\alpha$>0

$\frac{dE_P}{dE_A} < 1$

However, in the case of volume addition, the contact line pinning mode will be favored over the constant advancing angle mode if the ratio is less than 1. This is true even though the ratio of the two energies is less than 1, since the change in energy is opposite in sign when compared to the case where the volume was decreasing. The droplet would prefer to gain volume with the contact line being pinned and a continuous increase in contact angle until $\theta_Y = \theta$ is satisfied. At $\theta_Y = \theta$, both modes are again equally favored. The droplet can adapt to volume addition in the constant advancing angle mode. However, if the contact line continues to be pinned decrease such that the contact angle gets differentially larger ($|d\alpha| \to 0$) than the Young's contact angle such that:

$d\alpha$<0, *i.e.* $\theta_Y < \theta$ as shown on Figure S2

$\frac{dE_P}{dE_A} > 1$

In such as case, the ratio will be greater than 1 and the constant advancing angle mode will be favored with the contact angle being the Young's contact angle ($\theta_Y = \theta + d\alpha,$ and $|d\alpha| \rightarrow 0$ implying $\theta_Y \sim \theta$).

Mixed Mode

During the mixed mode, both the contact angle and the base radius change. The volume change is a function of two variables and hence can be calculated as follows:

$$dV_M = \frac{\partial V}{\partial R} dk + \frac{\partial V}{\partial \theta} d\varphi$$

$$dV_M = \pi R^2(2 - 3\cos\theta + cos^3\theta)dk + \pi R^3(sin\theta - cos^2\theta sin\theta)d\varphi$$

Assuming that the change is the contact angle during the mixed mode is a fraction z of that during the contact line pinning mode:

$$d\varphi = z d\theta \qquad \text{(S15)}$$

NOTE: Alternately, the change in the major radius *dk* can be assumed to be a fraction of that during the contact line pinning mode also, however, the conclusion will be the same.

As can be seen from Eq. S15, $z = 0$ implies constant receding angle mode and $z = 1$ implies contact line pinning mode. Equating the volume change in the contact line pinning mode and the mixed mode to get a relation between *dk* and $d\theta$:

$$dV_P = dV_M$$

$$\pi R^3 \frac{(1 - 2cos\theta + cos^2\theta)}{sin\theta} d\theta = \pi R^2(2 - 3\cos\theta + cos^3\theta)dk + \pi R^3(sin\theta - cos^2\theta sin\theta)z d\theta$$

Hence, we obtain a relation between the contact angle change in the pinning mode and the major radius change in the mixed mode as follows:

$$dk = \frac{R(1 - 2cos\theta + cos^2\theta - zsin^4\theta)}{sin\theta(2 - 3\cos\theta + cos^3\theta)} d\theta \qquad \text{(S16)}$$

Similarly, the change in the spherical cap area can be calculated as follows:

$$dA_{lv,M} = \frac{\partial A}{\partial R}dk + \frac{\partial A}{\partial \theta}\, d\varphi$$

Using Eq. S15,

$$dA_{lv,M} = 4\pi R(1-\cos\theta)dk + 2\pi R^2(sin\theta)zd\theta$$

Substituting the value of *dk* from Eq. S16:

$$dA_{lv,M} = 4\pi R^2(1-\cos\theta)\frac{(1-2cos\theta+cos^2\theta-zsin^4\theta)}{sin\theta(2-3\cos\theta+cos^3\theta)}d\theta + 2\pi R^2(sin\theta)zd\theta \quad \text{(S17)}$$

The change in the solid-liquid area is:

$$dA_{sl,M} = 2\,\pi R sin^2\theta dk + 2\,\pi R^2 sin\theta cos\theta d\varphi$$

Using Eq. S15 and Eq. S16,

$$dA_{sl,M} = 2\,\pi R^2 sin\theta\frac{(1-2cos\theta+cos^2\theta-zsin^4\theta)}{(2-3\cos\theta+cos^3\theta)}d\theta + 2\,\pi R^2 zsin\theta cos\theta d\theta \quad \text{(S17)}$$

Hence, the total change in energy due to volume loss is:

$$dE_M = (\gamma_{sl}-\gamma_{sv})dA_{sl,M} + \gamma_{lv}\,dA_{lv,M}$$

For simplification, let us assume:

$$J = \frac{(1-2cos\theta+cos^2\theta-zsin^4\theta)}{(2-3\cos\theta+cos^3\theta)} \quad \text{(S18)}$$

Using Eq. S17 and Eq. S18,

$$dE_M = \Big[-2\,\pi R^2 Jsin\theta(\gamma_{sv}-\gamma_{sl}) - 2\,\pi R^2(\gamma_{sv}-\gamma_{sl})zsin\theta cos\theta + 4\pi R^2\gamma_{lv}\frac{J(1-\cos\theta)}{sin\theta} + 2\pi R^2\gamma_{lv}(sin\theta)z\Big]d\theta \quad \text{(S19)}$$

Using Eqs. S4, S8, S9, S18 and S19 and simple trigonometric manipulations, it can be shown that for any combinations of contact angle θ, Young's contact angle θ_Y, and the fraction *z* (Eq. S15), the energy change during the mixed mode is in between those during the contact line pinning mode and constant receding angle mode, *i.e.*, $dE_P \le dE_M \le dE_R$ or $dE_R \le dE_M \le dE_P$. Also, $dE_R = dE_M$ if $z = 0$ and $dE_P = dE_M$ if $z = 1$. As shown on Figure S2, all three quantities

are equal when the instantaneous contact angle θ is equal to the Young's contact angle θ_Y. As a result, the mixed mode is never preferred thermodynamically and one of the two extreme modes prevails.

In summary, the above mentioned thermodynamic argument is in line with the ideal case of a smooth homogenous surface wherein upon the volume addition, the contact line gets pinned and the contact angle increases until it reaches the Young's value. The contact angle remains constant afterwards even with further volume addition. Conversely, if liquid is withdrawn, the contact line becomes pinned and the contact angle continuously decreases until it reaches the Young's value remaining constant afterwards.

The above analysis can also be performed for droplets on heterogeneous surfaces leading to the results described by Eq. 1 to Eq. 8. As can be shown for heterogeneous surfaces too, only the contact line pinning mode and the receding (advancing) modes are possible. Hence, the mixed mode is not considered for the hysteresis model developed in the main text.

S2. Sample preparation

Sample numbers 1-6, run number 1: The samples were plasma cleaned for 40 seconds after the initial solvent cleaning. Plasma cleaning eliminates organic contaminants on the surfaces and enhances surface energies of the samples leading to vanishing small contact angles. However, as both the advancing and receding contact angles were very small and no appreciable differences between the two surfaces (SiO_2 and photoresist) could be made, the samples were then washed in iso-propyl alcohol (IPA) followed by rinsing with deionized water and blow drying with N_2. An appreciable increase in the advancing contact angles on both baseline surfaces was observed. Nonetheless, the contact angles were still evolving with continued exposure to the ambient. In order to demonstrate the need for *in-situ* baseline contact angle calibration, experiments were started in a random order after the above mentioned cleaning procedure. Even though the surface energies between samples were different due to slight variations in the IPA and water rinse time as well as the time lag between sample cleaning and experiments, *in-situ* baseline contact angle measurement ruled out any discrepancy that could arise due to the experimental procedure.

Sample numbers 1-6, run number 2: The samples were re-investigated six hours after the first set of measurements (run number 1) without any solvent cleaning. N_2 was used to get rid of dust, if any.

Sample numbers 7-12, run number 1: Same as run number 1 for sample numbers 1-6.

Sample numbers 7-12, run number 2: The samples were plasma cleaned for 40 seconds after the initial solvent cleaning. The samples were then investigated randomly after an hour period without any exposure to IPA and water.

Sample numbers 13-24: The silanized samples were washed in iso-propyl alcohol and water and dried in N_2 before the start of each experiment. Plasma cleaning was not carried out since could potentially affect silane coating.

S3. Algorithm for modeling droplet evolution

The different stages of the computational methodology adopted to obtain the prediction results shown on Figure 9 and Figure 12 are discussed. If the initial droplet state and the volume addition rate were known, the energy ratio was computed at each time increments in order to decide the preferred mode of droplet evolution (constant advancing angle mode and contact line pinning mode):

$$\frac{dE_P}{dE_A} = \left[\frac{2 - 3\cos\theta_t + cos^3\theta_t}{-cos\theta_{eff,t}\, sin^2\theta_t \;+\; 2(1 - cos\theta_t)}\right] \tag{S20}$$

$$\text{where } cos\theta_{eff,t} = f_{eff,t}cos\theta_{1,A} + (1 - f_{eff,t})cos\theta_{2,A} \tag{S21}$$

Here, the starting value of $f_{eff,t=0}$ was assumed to be the same as the area fraction:

$$f_{eff,t=0} = (cos\theta_{t=0} - \cos\theta_{2,A})/(cos\theta_{1,A} - \theta_{2,A}) \tag{S22}$$

Even though the starting value was not exactly known and Eq. S22 is an assumption, the value of f_{eff} was updated almost instantaneously so that the starting value to be inconsequential to affect the outcome of the simulations. This assumption was validated by changing the initial condition on f_{eff} and re-running the complete simulations. The droplet evolution in all cases was very similar except for the first few seconds where the f_{eff} adjusted quickly to reach a quasi-steady state. Simple trigonometric manipulations can be performed to show that if $\theta_t < \theta_A$ based on Eq. 8, the ratio as per Eq. S20 was be less than 1 and the contact line pinning mode was favored. Based on the value of the differential volume, the incremental change in contact angle was calculated as per Eq. S2 (an equivalent case for homogenous surface). It should be noted here that the net rate of change of volume was equal to the difference of the addition rate by the dispensing system and evaporation rate, and hence the change in volume with time curve was not exactly linear even during the liquid addition phase. The change in the droplet major radius and hence the liquid-vapor area was then calculated using Eq. S1 and Eq. S3. At this point, the geometry of the droplet at the next time

interval was defined. However, in order to proceed with similar exercise (Eqs. S20-S22) for the next time step, the value of f_{eff} was required to be updated. The current value of the f_{eff} can be derived by differentiating Eq. S22 as follows:

$$f_{eff,t+\Delta t} = f_{eff,t} + df_{eff,t} = f_{eff,t} - \frac{sin\theta_t}{cos\theta_{1,A} - cos\theta_{2,A}} d\theta_t \quad \text{(S23)}$$

At this stage, all the information pertaining to geometry as required to advance the simulation was known and hence calculations as per Eq. S20-S23 could be performed repeatedly. Once the contact angle reached the advancing value corresponding to f_{eff}=0, the ratio as prescribed by Eq. S20 was greater than 1 and the constant advancing contact angle mode was preferred. In such a case, Eq. S5 to Eq. S7 was used until the end of liquid addition step. Once the liquid addition time was over, the droplet evaporated and the differential volume as calculated using Eq. S25 was negative. As a result, a ratio greater than 1 as prescribed by Eq. S20 (denominator energy change corresponds to receding mode for such a case) thermodynamically suggested a contact line pinning mode. The algorithm as prescribed by Eqs. S20-S22 along with appropriate geometry updates per Eq. S1, Eq. S3 and Eq. S4 were similarly performed to advance the simulation. As can be seen from Eq. S23, the fraction of the contact line on "1" continued to increase until it matched f_{max} for circular defects. When f_{eff}=f_{max}, the energy change ratio was smaller than 1 and the droplet started to recede without any change in the contact angle until complete evaporation.

S4. Contact line pinning time

Derivation: We now derive the equation for calculating the contact line pinning time. The rate of evaporation of a droplet on a substrate was defined by the classical model of Bourges-Monnier and Shanahan[14a]:

$$\frac{dV}{dt} = -\frac{4\pi RD}{\rho_l}(c_o - c_\infty)f(\theta), \text{ where } f(\theta) = \frac{-cos\theta}{2log_e(1-cos\theta)} \quad \text{(S24)}$$

In order to calculate the time that a droplet spent in the contact line pinning mode, the volume change during the pinning mode (S2) was equated to Eq. S24 as follows:

$$\pi R^2 \frac{(1-2cos\theta+cos^2\theta)}{sin\theta} d\theta = --\frac{4\pi D}{\rho_l}(c_o - c_\infty)f(\theta)dt$$

The number of variables is reduced from three to two by using the fact that the base radius is constant during the pinning mode ($Rsin\theta = R_o sin\theta_A$). Here, the advancing contact angle was used since the contact angle at the start of contact line pinning mode was the advancing angle of the droplet.

$$R_o^2 sin^2\theta_A \frac{(1-2cos\theta+cos^2\theta)}{4f(\theta)\, sin^3\theta} d\theta = -\frac{D}{\rho_l} c_o(1-RH)dt$$

Integrating the above equation where the limits on the contact angle for the contact line pinning time was the advancing and the receding contact angles, we got:

$$R_o^2 sin^2\theta_A \int_{\theta_A}^{\theta_R} \frac{(1-2cos\theta+cos^2\theta)}{4f(\theta)sin^3\theta} d\theta = -\frac{D}{\rho_l} c_o(1-RH) \int_o^t dt$$

No analytical solution was possible, however, the parametric effects of the diffusivity of the vapor, liquid density, relative humidity, and the initial droplet major radius can be perceived from the following equation:

$$t = \frac{R_o^2 \rho_l}{D c_o (1-RH)} F(\theta_A, \theta_R) \text{ where } F(\theta_A, \theta_R) = sin^2\theta_A \int_{\theta_A}^{\theta_R} \frac{(1-2cos\theta+cos^2\theta)}{4f(\theta)sin^3\theta} d\theta \quad \text{(S25)}$$

Here, *F* is a function of the advancing and receding contact angles and can be computed numerically.

Discussion: The knowledge of contact line pinning time is required to develop guidelines for performing contact angle hysteresis measurement studies. Contact angle hysteresis measurement studies rely on one of the three approaches: (a) droplet sliding on inclined surface, (b) natural evaporation, and (c) forced liquid withdrawal using syringe needle. Droplets sliding on inclined surfaces require large tilt angle and are difficult to achieve on surfaces with high hysteresis. Moreover, the imaging equipment is required to be moved along with the droplets if a considerable data acquisition time is required to establish constant advancing and receding angle modes. On the other hand, even though natural evaporation is preferred over forced liquid withdrawal as any modifications due to the withdrawal rate is minimal, the later liquid removal methodology is usually adopted if the droplet size is large (longer evaporation times for natural evaporation makes data storage expensive and analysis time intensive).

As an example, Figure S3 shows that for a microliter droplet under the same conditions and surface as in Figure 9, the proposed model predicts that more than 10 minutes will be required for the droplet to attain the constant receding mode (Eq. S25). As a result, even with such high hysteresis, the rate of change of contact angle (~0.1^{o}/sec) during the contact line pinning mode will be much smaller than the experimental uncertainty limits. Considering that for such large droplets, the contact line velocity even in the receding mode will be very small under natural evaporation, if not paid appropriate attention, the droplets during the pinning mode can be falsely perceived to be in receding mode unless the contact line is closely monitored with high resolution imaging techniques. Clearly, the above model can be used as a tool to estimate the pinning time and decide the feasibility of using natural evaporation for the determination of the receding contact angle on surfaces. In case liquid is to be removed using a syringe and needle, the dependence of the pinning

time on withdrawal rates can be used to wisely decide the appropriate data acquisition rates and times.

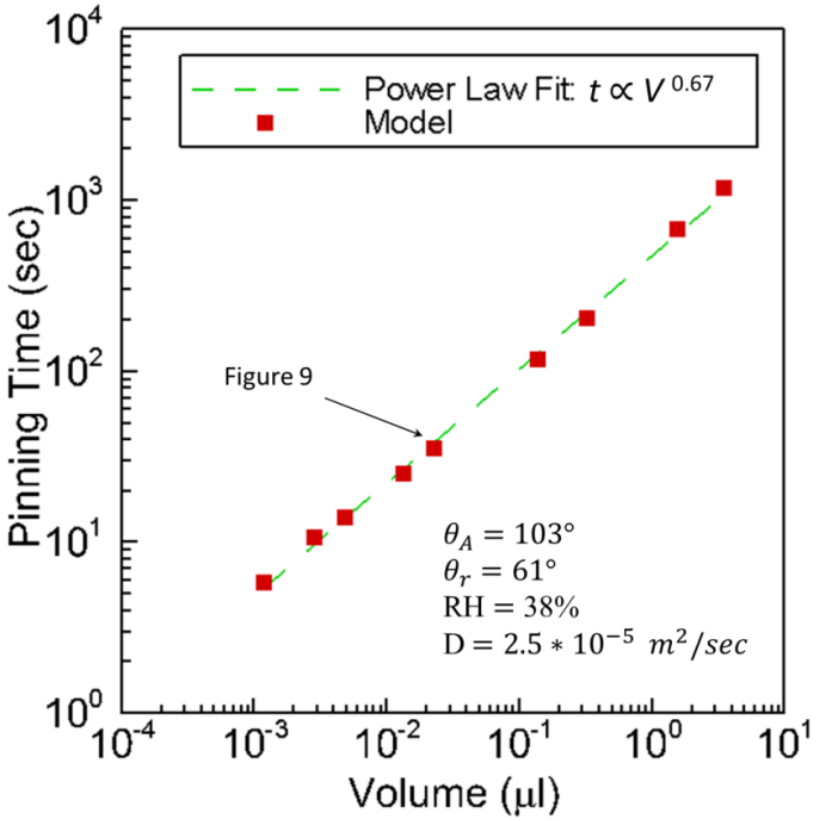

Figure S3. Prediction of contact line pinning time versus volume for sample number 16.